Corrosion and Electrocatalytic Behaviors of Additively Manufactured INCONEL 718 Alloy in pH Adjusted 3.5% NaCl Solutions at Room Temperature

A Thesis
Presented in Partial Fulfillment of the Requirements for the
Degree of Master of Science
with a
Major in Materials Science and Engineering
in the
College of Graduate Studies
University of Idaho
by
Thomas Thuneman

Major Professor: Krishnan Raja, Ph.D.

Committee Members: Indrajit Charit, Ph.D.; Michael Maughan, Ph.D.

Department Administrator: Indrajit Charit, Ph.D.

December 2020

Authorization to Submit Thesis

This thesis of Thomas Thuneman, submitted for the degree of Master of Science with a major in Materials Science and Engineering and titled "Corrosion and Electrocatalytic Behaviors of Additively Manufactured INCONEL 718 Alloy in pH Adjusted 3.5% NaCl Solutions at Room Temperature," has been reviewed in final form. Permission, as indicated by the signatures and dates below, is now granted to submit final copies to the College of Graduate Studies for approval.

Major Professor: _____ Date: _____
                            Krishnan Raja, Ph.D.

Committee Members: _____ Date: _____
                            Indrajit Charit, Ph.D.

                             _____ Date: _____
                            Michael Maughan, Ph.D.

Department
Administrator: _____ Date: _____
                            Indrajit Charit, Ph.D.

Abstract

INCONEL 718 is a heat treatable Ni-Fe-Cr-Mo alloy used in a wide range of temperatures (23 – 977 K) because of its superior strength, toughness, and resistance to creep and corrosion. It is a material of choice for components of aircraft engines, gas turbines, oil drilling equipment, nuclear reactors, cryogenic tanks, heat exchangers, and liquid fueled rockets. Additive manufacturing (AM) techniques are implemented to manufacture near net shape components out of INCONEL 718 because of the complexity of design of the components and to minimize the machining cost. Selective laser melting (SLM) is one of the AM techniques which uses a laser beam to selectively melt a layer of alloy powder. The layered melting helps build the required 3D shape of a component. The high energy density melting also leads to very high cooling rates in the order of 106ºC/s. Therefore, SLM process results in isotropic, fine grained microstructures with metastable phases that are not usually obtained in conventional manufacturing processes such as casting or forging. The objectives of this study are to: a) evaluate the corrosion behavior of additively manufactured INCONEL 718 in 3.5% NaCl solutions with varying pH (1.25, 6.25, and 12.25) and correlate with different microstructural conditions obtained by hot isostatic pressing (HIP), and two-step aging treatments; b) compare the corrosion resistance of the additively manufactured material with the conventional wrought material, and c) investigate the electrocatalytic behavior of AM-718 material for hydrogen and oxygen evolution reactions for possible applications as electrodes in water electrolyzers.

Cyclic polarization, potentiostatic, and electrochemical impedance spectroscopy measurements were carried out on the INCONEL 718 alloy specimens in four different microstructural conditions. The results showed that the as-printed specimens showed better corrosion resistance than the wrought material in the acidic chloride solution. HIP specimens exhibited superior corrosion resistance to the as-printed ones. Heat treatment resulted in a reduction of overall corrosion resistance. The Tafel slopes for the HER were higher in the as-received samples compared to their heat-treated counterparts in all the pH conditions with samples tested in a basic environment showing the lowest Tafel slopes. The room temperature corrosion properties are relevant for oil field applications, and electrochemical machining of Inconel 718.

Acknowledgements

I would foremost like to thank Dr. Krishnan Raja for his guidance and support though my academic career at the University of Idaho, both as my undergraduate academic advisor, and especially during my Master's program.

I would also like to thank Dr. Indrajit Charit and Dr. Michael Maughan for agreeing to sit on my thesis committee.

I would like to acknowledge Charles Cornwall and Brian Petty in the machine shop for helping me in cutting and preparing my samples for analysis, as well as Dr. Thomas Williams for his assistance in scanning electron microscopy and X-ray diffraction.

Finally, I would like to acknowledge my fellow graduate students who have aided me in the laboratory with experiments, with learning new procedures and methods, and help with general schoolwork. Thank you all.

Dedication

To my parents, for your ceaseless patience, love, and support. For all that you have done.

Thank you.

Table of Contents

List of Figures

List of Tables

Chapter 1: Background and Literature Review for Corrosion and Inconel 718

1.1 Corrosion

Corrosion is a natural electrochemical process constituting the destructive attack and oxidation of a metal to reduce the material to a more thermodynamically stable state. In general, corrosion occurs either in a uniform capacity, over the entirety of the exposed surface of the material, or in smaller areas and regions, depending on localized conditions. As corrosion progresses, the base metal is weakened, causing an overall loss in material structural integrity and increasing fatigue. These effects in turn accelerate the rate of corrosion [1].

Pitting is a highly damaging form of localized corrosion that occurs in passive metals. It is particularly pervasive in stagnant marine environments with high concentrations of chloride (Cl^-), or in the presence of other halide ions such as fluoride (F^-), bromide (Br^-), and iodide (I^-). Pitting corrosion is characterized, as the name suggests, by the formation of holes, or pits, in the material that leads to material failure.

A metal in a passive state indicates the formation of an inert protective film across the surface, resulting in reduced chemical reactivity in the metal. The thickness of the film is in the range of a few nanometers and can form naturally under varying environmental conditions, or can be artificially added, increasing the material's uniform corrosion resistance. Pitting corrosion is caused by a defect, break, or other anomaly in this film, that create anodic sites on the metal surface, allowing for material dissolution [2]. This anodic reaction is represented by the following equation:

$$M \rightarrow M^{n+} + ne^- \tag{1.1}$$
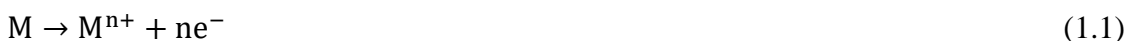
where M is the reacted metal. The metal's passive surface acts as cathode in the exchange with the balancing oxygen reduction reaction is shown as:

$$O_2 + 2H_2O + 4e^- \rightarrow 4OH^- \tag{1.2}$$

As dissolution continues and the pit deepens, M^+ ions released from the point of corrosion coalesce in the pit area lowering the pH and creating a localized acidic environment. A balance is created between the ion concentration due to material dissolution and mass transfer from the

pit due to material diffusion and electromigration. As long as a critical concentration within the pit is maintained (dependent on material, environment, etc.), pitting continues and a self-sustaining system is created and corrosion may continue until the metal is fully perforated. If critical concentration is not maintained, the pit repassivates [3].

The devastating effects of corrosion necessitate the continued research and development of novel metal alloys and component manufacturing that can better withstand material degradation. In particular, superalloys have been developed for use in extreme environments and applications.

1.2 Superalloys

Superalloys are high-performance metal alloys characterized by high material strength and fracture toughness, long fatigue life, and exceptional resistance to high temperature oxidation and corrosion. They have been developed for, and used extensively in gas turbine blades and in the construction of jet and rocket engines, and in other severe and highly corrosive environments. There are three primary families of superalloys: cobalt-based, iron-based, and nickel-based. [4, 5, 6].

In general cobalt-based superalloys exhibit higher hot-corrosion resistance compared to nickel-based and iron-based alloys. However, precipitates formed during strengthening lack the high temperature strength improvements that nickel alloys undergo and are therefore usually inferior in resistance to creep and stress rupture [4].

Iron-based superalloys are generally the least expensive to produce and behave similarly to nickel alloys while benefitting from increased wear resistance due to the hardening effects of excess carbon content.

Nickel-based superalloys contain at least 50 percent nickel by weight. In addition to high oxidation resistance, these alloys are generally preferred in turbine engines due to high stress rupture strength and superior creep resistance at higher temperatures. A common subgroup in this category consists of nickel-iron-based (Ni-Fe) alloys which show low thermal expansion at high temperatures, making them ideal for precision moving parts. INCONEL 718 (IN718)

is one of the most widely used in aerospace applications [4]. This alloy is described in further detail below.

1.3 INCONEL 718

IN718 is a Ni-Fe based superalloy initially developed in the early 1960s by INCO Huntington Alloys (now Special Metals Company) specifically for gas turbine components [7]. It consists primarily of nickel, chromium, and iron with smaller quantities of niobium, molybdenum, titanium, and aluminum. The nominal weight percentage of these major alloying elements are shown in Table 1.1. Other elements may be present in trace amounts.

Table 1.1. Inconel 718 Nominal Composition [8].

Element	Nickel	Chromium	Iron	Niobium	Molybdenum	Titanium	Aluminum
Wt %	50-55	17-21	15-20	4.75-5.50	2.80-3.30	0.65-1.15	0.20-0.80

IN718 exhibits high strength due to hardening facilitated by the added niobium, titanium, and aluminum, which form intermetallic hardening precipitates γ'' (Ni_3Nb, body-centered tetragonal crystal) and γ' (Ni_3(Ti, Al), simple cubic crystal) respectively. IN718 can generally be used at a wide range of temperatures, from cryogenic to 650°C [9].

High iron content (15-20 wt%) aids in cost reduction and improves material malleability, but impairs overall high temperature oxidation resistance [10]. Molybdenum serves to increase the alloy's mechanical resistance through solid solution hardening. The high chromium content and the nickel crystallize together as a γ phase (face centered cubic) and contribute to an excellent resistance to oxidation and corrosion at high temperatures [11].

Because its high strength and corrosion resistance, this alloy has found particular application in high stress environments, especially in the aerospace and energy industries where it is employed in turbine blades, aircraft and rocket engines, and for nuclear reactor components. IN718 has also found various use in oil and gas production.

Conventionally created IN718 parts demonstrate poor machinability due to the high strength of the alloy, and are also subject to the standard uneven melt issues that may stem from wrought

and casted fabrications. Because of these limitations, and the precision needed to fabricate detailed aerospace components, IN718 has been the subject of much research and development regarding metallurgical additive manufacturing as an alternative production process.

1.4 Additive Manufacturing

Traditionally, metal parts have been produced using standard casting and forging (wrought) techniques. Metal casting consists of melting alloy stock and inserting the molten metal into a mold of the desired component to cool. Upon solidification, the piece is extracted and the mold discarded. Forging processes shape solid stock though impact working, pressing, and extrusion to achieve a formed part.

In addition, milling techniques are also used for precise fabrication, in which unwanted material is removed by machine from a bulk piece, resulting in a precisely manufactured final product. Though this method is more exacting than forging or casting, it is much more time consuming and is ineffective with higher strength alloys that are resistant to tooling.

These methods may be prone to microstructure imperfections affecting alloy homogeneity created during the material melting and cooling processes and can have an unfavorable effect on the alloy's physical and mechanical properties. Additive manufacturing (AM) has been developed to help mitigate these concerns.

AM is a process in which a material element is created incrementally using one of a vast array of three-dimensional (3D) printing techniques and has been developed, and applied in many different industries throughout the world. Recently, there has been an increase in the advancement of AM as a practical method in the precise production of metallic components, and as a viable alternative to more conventionally constructed ones. There are two primary methods of AM for metal components, depending on the state of the material feedstock; wire-feed, and powder-based metallurgy.

Wire-feed methods utilize metal wire delivered through a nozzle close to the build surface to supply the alloy material, where it is melted using an energy source (laser, arc-welding, or electron beam) and allowed to resolidify. Each new pass deposits more material onto the

constructed component, which is built upward in layers. One of the most common wire-feed AM methods is Directed Energy Deposition (DED), shown in Figure 1.1.
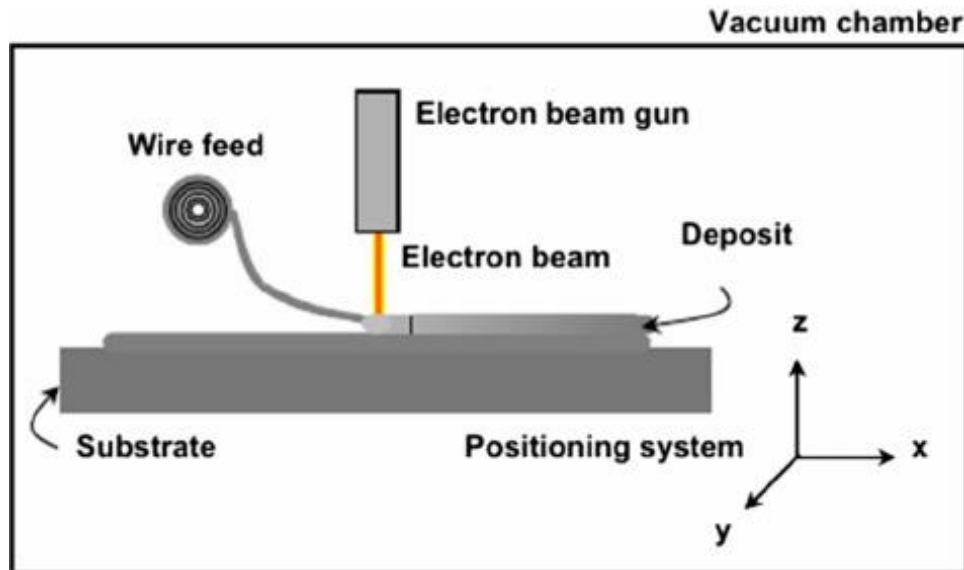
Figure 1.1. *Diagram of wire-feed DED using electron beam energy source [12]*

Powder-based AM use powdered alloy stock. The powder may be delivered by nozzle directly to the build surface, similar to wire-feeding, or supplied incrementally from a powder bed (powder-bed fusion). In particular, Selective Laser Melting (SLM) has found widespread use, and is the primary method of fabrication for the samples researched in this study [12].

SLM was first developed and used in the 1990s by Fraunhofer Institute of Laser Technology [13]. It is one of a variety of laser-based powder bed AM methods in which three-dimensional metal parts are rapidly constructed in layers from a computer aided design (CAD) using a focused laser beam to melt a powdered metal alloy that is continually redistributed over the work area after each successive layer is created [8, 14, 15, 16]. The powder particles are generally less than 100 µm in diameter and the layer thickness commonly ranges from 20-100 µm, with optimum parameters set for each build [17]. The fabrication process is completed within an airtight build chamber subjected to the flow of an inert gas (usually argon or nitrogen) to prevent material oxidation and remove condensation produced by the melting powder [18].

Because the laser, and therefore the heat, is concentrated on a relatively small and localized spot on the build surface, the precise creation of detailed and complex components is possible,

with greater alloy homogeneity and finer microstructure than can be achieved through casting and forging while eliminating the complications that arise from extended melt and solidification times. In addition, the additive construction greatly reduces the wasted product that is created through other milling techniques [19]. Figure 1.2 shows the major components of this process.
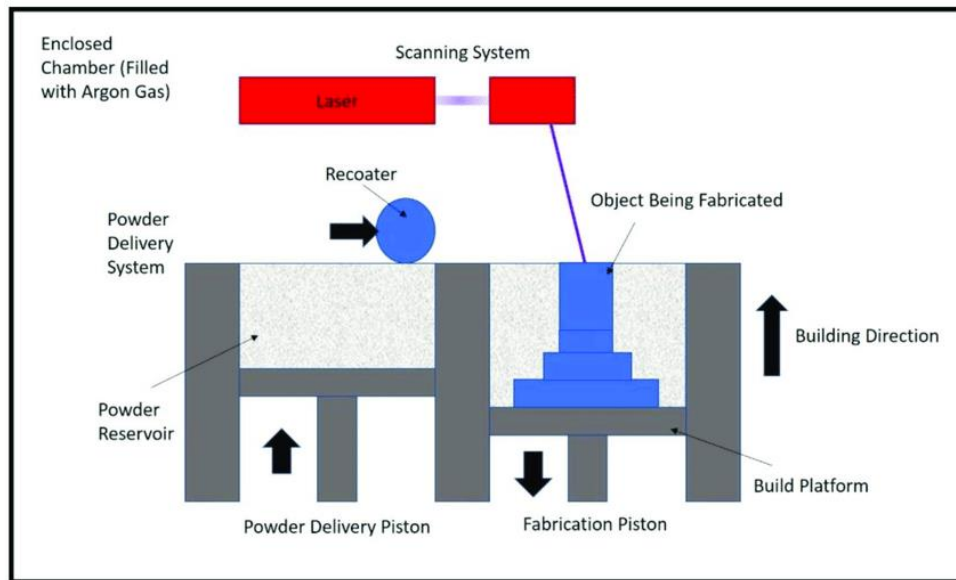
Figure 1.2. Diagram of typical SLM process [20]

There are numerous factors throughout the SLM manufacturing process that will affect the final material, however the primary concern regards material porosity resulting from voids in the microstructure created during the powder sintering process. A more porous material is less dense and has an inconsistent microstructure, proving detrimental to the material's overall mechanical properties. Especially under common loading, pores may reduce the overall fatigue strength of the component by acting as stress concentrators that may introduce premature cracking [16]. Furthermore, the uneven material surface created by surface pores may disrupt the protective passive film and allow for greater corrosion susceptibility.

There are various ways to reduce porosity and increase the density of the completed part during SLM construction. These parameters vary with different materials and include laser scanning speed and spot size (width of the beam), hatch distance (distance between adjacent beam scans), stock particle size, and individual layer thickness. In addition, there are numerous post-

fabrication methods used in porosity reduction. In particular, the hot isostatic pressing (HIP) method has become a favored means for strengthening powder-based additively manufactured components.

1.5 Hot Isostatic Pressing

HIP was originally invented in the 1950s by the Battelle Memorial Institute for diffusion welding of nuclear reactor components and was soon found to be an excellent method of powder consolidation and eliminating voids within the material microstructure [21].

In this process, a combination of high heat and hydrostatic pressure is simultaneously applied to a powder compact in order to increase material density and refine its microstructure. The component is contained within a capsule then placed into a pressure vessel that is subjected to a uniform expansion of a heated inert gas (commonly argon). The heated gas exerts great pressure on the component, compacting the material and eliminating voids in the microstructure. Typical applied temperature and achieved pressure range from 500-2000°C and 20-300 MPa respectively. HIP can achieve nearly 100 percent material densification faster than other densification methods while maintaining lower grain size, as pressure has negligible effect on the rate of grain growth [15]. In a comprehensive study of HIP optimization, Lee et al [22] determined that the ideal process parameters for HIP of IN718 consisted of a temperature of 1180°C with 175 MPa and four hours of soaking time. This allowed for superior homogenous composition, uniform grain size, and improved material mechanical properties.

A diagram of standard HIP unit is shown in Figure 1.3.
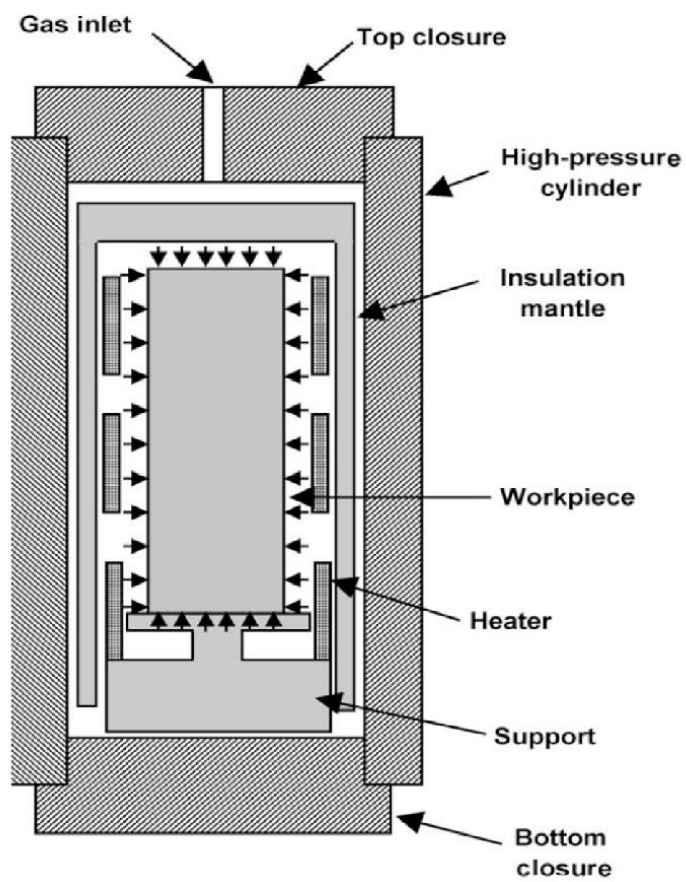
Figure 1.3. Schematic of common HIP apparatus [23]

1.6 References

[1] S. Hiromoto, "Corrosion of Metallic Biomaterials," in *Metals for Biomedical Devices*, 2nd ed., M. Niinomi, Ed., Cambridge, Woodhead Publishing, 2019, pp. 131-152.

[2] Z. Ahmad, "Types of Corrosion: Materials and Environments," in *Principles of Corrosion Engineering and Corrosion Control*, amsterdam, Elsevier, 2006, pp. 120-270.

[3] M. Kaneko and H. Isaacs, "Effects of Molybdenum on the Pitting of Ferritic- and Austenitic-Stainless Steels in Bromide and Chloride Solutions," *Corrosion Science,* vol. 44, no. 8, pp. 1825-1834, August 2002.

[4] A. P. Mouritz, "Superalloys for Gas Turbine Engines," in *Introduction to Aerospace Materials*, A. P. Mouritz, Ed., Cambridge, Woodhead Publishing Limited, 2012, pp. 251-267.

[5] S. Manikandan, D. Sivakumar and M. Kamaraj, "Physical Metallurgy of Alloy 718," in *Welding the Inconel 718 Superalloy*, Amsterdam, Elsevier, 2019, pp. 1-19.

[6] T. A. Tejedor, "Gas Turbine Materials Selection, Life management and performance Improvement," in *Powerplant Mangement and Performance Improvement*, J. E. Oakey, Ed., Cambridge, Woodhead Publishing Limited, 2011, pp. 330-419.

[7] H. Qi, "Review of INCONEL 718 Alloy: Its History, Properties, Processing and Developing Substitutes," *Journal of Materials Engineering,* vol. 2, no. 8, pp. 92-100, 2012.

[8] D. Deng, R. L. Peng, H. Brodin and J. Moverare, "Microstructure and Mechanical Properties of Inconel 718 Produced by Selective Laser Melting: Sample Orientation Dependence and Effects of Post Heat Treatments," *Materials Science and Engineering,* vol. 713, pp. 294-306, 2018.

[9]   S. Luo, W. Huang, H. Yang, J. Yang, Z. Wang and X. Zeng, "Microstructural Evolution and Corrosion Behaviors of Inconel 718 Alloy Produced by Selective Laser Melting Following Different Heat Treatments," *Additive Manufacturing,* vol. 30, p. 100875, December 2019.

[10] R. Sahraeian, H. Omidvar, S. M. Mehdi Hadavi, S. Shakerin and V. Maleki, "An Investigaion on High-Temperature Oxidation and Hot Corrosion Resistance Behavior of Coated TLP (Transient Liquid Phase)-Bonded IN738-LC," *Transactions of the Indian Institute of Metals,* vol. 71, no. 12, pp. 2903-2918, October 2018.

[11] A. Thomas, M. El-Wahabi, J. M. Cabrera and J. M. Prado, "High Temperature Deformation of Inconel 718," *Journal of Materials Processing Technology,* vol. 177, no. 1-3, pp. 469-472, 2006.

[12] D. Ding, Z. C. D. Pan and H. Li, "Wire-Feed Additive Manufacturing of Metal Components: Technologies, Developments, and Future Interests," *The International Journal of Advanced Manufacturing Technology,* vol. 81, pp. 465-481, May 2015.

[13] O. Neikov, "Powders for Additive Manufacturing Processing," in *Handbook of Non-Ferrous Metal Powders (2nd Eddition)*, O. Neikov, Ed., Amsterdam, Elesevier, 2019, pp. 373-399.

[14] Q. Jia and D. Gu, "Selective Laser Melting Additive Manufacturing of Inconel 718: Superalloy Parts: Densification, Microstructure and Properties," *Journal of Alloys and Compounds,* vol. 585, pp. 713-721, 2014.

[15] L. F. Francis, "Powder Processes," in *Materials Processing: A Unified Approach to Processing of Metals, Ceramics and Polymers*, Amsterdam, Elsevier Inc., 2016, pp. 343-314.

[16] W. Tillmann, C. Schaak, J. Nellesen, M. Schaper, M. E. Aydinoz and H. K. -P, "Hot Isostatic Pressing of IN718 Components Manufactured by Selective Laser Melting," *Additive Manufacturing,* vol. 13, pp. 93-102, January 2017.

[17] H. K. Rafi, N. V. Karthik, H. Gong, T. L. Starr and B. E. Stucker, "Microstructures and Mechanical Properties of Ti6Al4V Parts Fabricated by Selective Laser Melting and Electron Beam Melting," *Journal of Materials Engineering and Performance,* vol. 22, no. 12, pp. 3872-3883, 2013.

[18] S. Sun, M. Brandt and M. Easton, "Powder Bed Fusion Processes: An Overview," in *Laser Additive Manufacturing*, M. Brandt, Ed., Cambridge, Woodhead, 2017, pp. 55-77.

[19] G. A. Rao, M. Kumar, M. Srinivas and D. S. Sarma, "Effect of Standard Heat Treatment on the Microstructure and Mechanical Properties of Hot Isostatically Pressed Superalloy Inconel 718," *Materials Science and ENgineering: A,* vol. 355, no. 1-2, pp. 114-125, August 2003.

[20] L. Jiao, Z. Y. Chua, S. K. Moon, J. Song, G. Bi and H. Zheng, "Femtosecond Laser Produced Hydrophobic Hierarchial Structures on Additive Manufacturing Parts," *Nanomaterials,* vol. 8, no. 8, pp. 1-10, August 2018.

[21] D. F. Heaney and C. Binet, "Hot Isostatic Pressing (HIP) of Metal Injection Molding (MIM)," in *Handbood of Metal Injection Molding (2nd Edition)*, D. F. Heaney, Ed., Cambridge, Woodhead Publishing, 2019, pp. 195-202.

[22] S.-C. Lee, S.-H. Chang, T.-P. Tang, H.-H. Ho and J.-K. Chen, "Improvenemt in the Microstructure and Tensile Properties of Inconel 718 Superalloy by HIP Treatment," *Materials Transactions,* vol. 47, no. 11, pp. 2877-2881, 2006.

[23] M. H. Bocanegra-Bernal, "Hot Isostatic Pressing (HIP) Technology and its Applications to Metals and Ceramics," *Journal of Materials Science,* vol. 39, no. 21, pp. 6399-6420, 2004.

Chapter 2 Background and Literature Review for Electrocatalysts

2.1 Introduction

With continuous advances in modern technologies, there is an ever-increasing demand for more energy. Traditional energy sources primarily include coal, natural gases, and petroleum-based products (common fossil fuels), however there is growing concern over these sources regarding consumption and general sustainability. In addition, there is an icreasing awareness of detrimental effects of fossil fuel pollution on the population, and overall impact on the environment. Therefore, there is a great desire to develop reliable, clean, and renewable energy alternatives. A key topic of interest concerns the production and exploitation of hydrogen for industrial fuel, and in the operation of hydrogen-based batteries and fuel cells.

There are three reactions associated with hydrogen production processes: hydrogen evolution reaction (HER), oxygen reduction reaction (ORR), and oxygen evolution reaction (OER). The fundamental reaction equations are shown:

$$2H^+ + 2e^- \rightarrow H_2 \qquad\qquad \text{HER} \qquad\qquad\qquad (2.1)$$

$$4H^+ + O_2 + 4e^- \rightarrow 2H_2O \qquad \text{ORR} \qquad\qquad\qquad (2.2)$$

$$2H_2O \rightarrow O_2 + 4e^- + 4H^+ \qquad \text{OER} \qquad\qquad\qquad (2.3)$$

Mechanisms for HRR, ORR, and OER in alkaline and acidic environments are subsequently shown and explained thoroughly.

2.2 Hydrogen Evolution Reaction (HER)

HER results in the production of hydrogen gas (H_2) and is a key topic of interest in electrochemistry with numerous practical applications, primarily including use in metal hydride batteries, the research and development of hydrogen fuel cells, and the production of hydrogen gas for industrial use through water electrolysis.

HER during corrosion is cathodic and follows the known Volmer-Heyrovsky-Tafel mechanism to release H_2. In alkaline environments this is given by [1]:

$$M + H_2O + e^- \rightarrow MH_{ad} + OH^- \qquad \text{Volmer} \qquad (2.4)$$

$$MH_{ad} + H_2O + e^- \rightarrow M + H_2 + OH^- \qquad \text{Heyrovsky} \qquad (2.5)$$

$$MH_{ad} + MH_{ad} \rightarrow 2M + H_2 \qquad \text{Tafel} \qquad (2.6)$$

In acidic environments, the Volmer and Heyrovsky equations are modified slightly [2]:

$$M + H_3O^+ + e^- \rightarrow MH_{ad} + H_2O \qquad \text{Volmer} \qquad (2.7)$$

$$MH_{ad} + H_3O^+ + e^- \rightarrow M + H_2 + H_2O \qquad \text{Heyrovsky} \qquad (2.8)$$

M is the electrocatalyst metal (electrode) and MH_{ad} is the hydrogen adsorbed on the surface of the electrode. HER initiates with the adsorption of a hydrogen atom (Volmer reaction) followed by an electrochemical recombination of an adsorbed hydrogen atom with an H^+ ion from the electrolyte (Heyrovsky reaction) and/or a chemical recombination of two adsorbed hydrogen atoms (Tafel reaction), to form hydrogen gas (H_2). The Heyrovsky and Tafel reactions may occur concurrently or separately in a system by following either the Volmer-Heyrovsky or Volmer-Tafel pathway [2, 3].

In both pathways, the hydrogen adsorption (Volmer) step is crucial requiring an electrocatalyst that will best facilitate the adsorption process. Platinum metal is generally considered the best known electrocatalyst for HER as hydrogen adsorption free energy on platinum is near the thermoneutral state [3].

2.3 Oxygen Reduction Reaction (ORR)

ORR is another cathodic half-reaction that may occur during the corrosion process that consists of the reduction of oxygen gas (O_2) to either hydroxide (OH^-) in basic solutions, or liquid water (H_2O) in acidic solutions. It is vitally important in energy-based systems, with particular applications in fuel cells and batteries. Generally, in aqueous environments, ORR may occur in one of two pathways: a four-electron transfer or a two-step two-electron transfer. Corresponding reactions in alkaline and acidic electrolyte solutions are shown below [4, 5].

In alkaline environments:

$$O_2 + 2H_2O + 4e^- \rightarrow 4OH^- \qquad \text{Four-electron Transfer} \qquad (2.9)$$

$$O_2 + 2H_2O + 2e^- \rightarrow HO_2^- + OH^- \qquad \text{Two-electron Transfer} \qquad (2.10)$$

$$H_2O + HO_2^- + 2e^- \rightarrow 3OH^- \qquad\qquad\qquad\qquad\qquad (2.11)$$

In acidic environments:

$$O_2 + 4H^+ + 4e^- \rightarrow 2H_2O \qquad \text{Four-electron Transfer} \qquad (2.12)$$

$$O_2 + 2H^+ + 2e^- \rightarrow H_2O_2 \qquad \text{Two-electron Transfer} \qquad (2.13)$$

$$H_2O_2 + 2H^+ + 2e^- \rightarrow 2H_2O \qquad\qquad\qquad\qquad\qquad (2.14)$$

Due to a higher required overpotential and slower reaction kinetics, ORR is generally considered the limiting step over HER in a system. Similar to HER, platinum is also the preferred electrocatalyst in ORR, but is not always practical [4].

2.4 Oxygen Evolution Reaction (OER)

OER concerns the production of oxygen gas molecules (O_2) through a four-step reaction process and is a primary mechanism in water splitting, as will be discussed in the next section. The OER reaction equations are given:

In a basic electrolytic solution [4, 6]:

$$S + OH^- \leftrightharpoons SOH + e^- \qquad\qquad\qquad\qquad\qquad (2.15)$$

$$SOH + OH^- \leftrightharpoons SO + H_2O + e^- \qquad\qquad\qquad\qquad (2.16)$$

$$SO + OH^- \leftrightharpoons SOOH + e^- \qquad\qquad\qquad\qquad\qquad (2.17)$$

$$SOOH + OH^- \leftrightharpoons S + O_2 + H_2O + e^- \qquad\qquad\qquad (2.18)$$

In an acidic electrolytic solution [4]:

$$S + H_2O \leftrightharpoons SOH + H^+ + e^- \qquad\qquad\qquad\qquad\qquad (2.19)$$

$$SOH \leftrightharpoons SO + H^+ + e^- \qquad\qquad\qquad\qquad\qquad\qquad (2.20)$$

$$SO + H_2O \leftrightharpoons SOOH + H^+ + e^- \qquad\qquad\qquad\qquad (2.21)$$

$$SOOH \leftrightharpoons S + O_2 + H^+ + e^- \qquad\qquad\qquad\qquad\qquad (2.22)$$

where S represents the active sites on the electrocatalyst.

Generally, OER is very sluggish due to more complex reaction kinetics. This leads to high overpotential in water splitting that proves detrimental to the efficiency of the process. Besides water splitting, OER is utilized as a key half-reaction in many fuel cells and rechargeable batteries [4], as well as in industrial applications including electroplating and electrowinning [7].

2.5 Water Splitting

H_2 may be produced through water splitting (electrolysis), a process in which an electric current is passed through water (H_2O) to fundamentally break down into hydrogen and oxygen. In water splitting, HER is the cathodic half-reaction and OER is the limiting corresponding anodic half-reaction.

The earliest demonstration of water splitting technology dates to AD 1800 when William Nicholson and Anthony Carlisle decomposed water into its oxygen and hydrogen components in England. In the same year, this was independently confirmed by Johann Wilhelm Ritter in Germany. One hundred years later, there were more than 400 industrial water electrolyzers in operation around the world [8, 9].

Industrial water splitting is generally enacted in a higher pH solution as an alkaline environment compared to an acidic environment, is much less corrosive to the electrocatalyst, and is less expensive to maintain [8]. In addition, an alkaline electrolyte allows for more efficient use of nonprecious electrocatalysts and favors the limiting oxygen evolution step, allowing for a faster reaction [10].

Fundamentally, in alkaline water electrolysis, two water molecules (H_2O) are reduced to one hydrogen molecule (H_2) and two hydroxyl ions (OH^-) at the cathode (HER process). The hydrogen escapes as a gas while the hydroxyl ions migrate to the anode and are discharged as one molecule of water and ½ molecule of oxygen (OER process). The oxygen recombines and escapes as a gas. This process is shown in the following reaction equations [9, 10]:

$$H_2O \rightarrow H_2 + 1/2\ O_2 \qquad\qquad \text{Total Reaction} \qquad\qquad (2.23)$$

$$2H_2O + 2e^- \rightarrow H_2 + 2OH^- \qquad\qquad \text{Cathode Reaction (HER)} \qquad\qquad (2.24)$$

$$2OH^- \rightarrow H_2O + 1/2\ O_2 + 2e^- \qquad\qquad \text{Anode Reaction (OER)} \qquad\qquad (2.25)$$
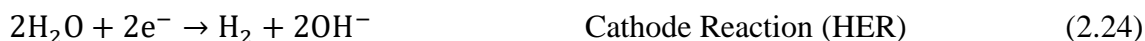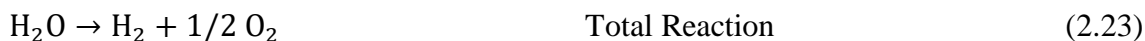
Because water itself is a poor conductor of electricity, electrolysis requires excessive overpotential to be efficient in pure water. Therefore, an electrolyte of a dissolved ionic species is added to increase the conductivity of the solution. In order for H_2 to be produced, the electrolyte must include a cation with a lower standard electrode potential than H^+.

Sea water, as a natural and abundant electrolyte, has been utilized as a source of H_2 through chloralkali electrolysis. This process primarily concerns the production of chlorine gas (Cl_2) and sodium hydroxide (NaOH); however, H_2 is a collected useful byproduct.

2.6 Electrocatalysts

The electrocatalyst used is an important factor in the viability and efficiency of the electrochemical reaction processes. Ideal electrocatalysts will maximize overall process efficiency and generally include pure or alloyed noble metals, such as the aforementioned platinum (Pt), as well as ruthenium (Ru), and palladium (Pd) because of the high overpotential needed. However high cost and scarcity prevent these metals from being practical choices in most circumstances, therefore there has been much research in finding low-cost alternative nonprecious alloys to act as an efficient electrocatalyst [3].

Nickel-based alloys have found considerable favor as a cost-effective material in HER applications due to high electrical conductivity and thermal stability, as well as excellent resistance to corrosion.

2.7 References

[1] N. Krstajic, M. Popovic, B. Grgur, M. Vojnovic and D. Sepa, "On the Kinetics of the Hydrogen Evolution Reaction on Nickel in Alkaline Solution: Part I. The Mechanism," *Journal of Electroanalytical Chemistry,* vol. 512, no. 1-2, pp. 16-26, October 2001.

[2] O. Azizi, M. Jafarian, F. Gobal, H. Heli and M. Nahjani, "The Investigation of the Kinetics and Mechanism of Hydrogen Evolution Reaction on Tin," *International Journal of Hydrogen Energy,* vol. 32, no. 12, pp. 1755-1761, August 2007.

[3] A. Eftekhari, "Electrocatalysts for Hydrogen Evolution Reaction," *International Journal of Hydrogen Energy,* vol. 42, no. 16, pp. 11053-11077, April 2017.

[4] V. Vij, S. Sultan, A. Harzandi, A. Meena, J. N. Tiwari, W.-G. Lee, T. Yoon and K. S. Kim, "Nickel–Based Electrocatalysts for Energy Related Applications: Oxygen Reduction, Oxygen Evolution, and Hydrogen Evolution Reactions," *ACS Catalysis,* vol. 7, no. 10, pp. 7196-7225, 2017.

[5] F. Si, Y. Zhang, L. Yan, J. Zhu, M. Xiao, C. Liu, W. Xing and J. Zhang, "Electrochemical Oxygen Reduction Reaction," in *Rotating Electrode Methods and Oxygen Reduction Electrocatalysts*, W. Xing, G. Yin and J. Zhang, Eds., Amsterdam, Elsevier B.V., 2014, pp. 133-170.

[6] T. Shinagawa and K. Takanabe, "Towards Versatile and Sustainable Hydrogen Production Via Electrocatalytic Water Splitting: Electrolyte Engineering," *ChemSusChem,* vol. 10, no. 7, pp. 1318-1336, 2017.

[7] O. Diaz-Morales and F. Calle-Vallejo, "Oxygen Evolution Reaction Catalyzed by Cost-Effective Metal Oxides," Elsevier, 2018.

[8] W. Kreuter and H. Hofmann, "Electrolysis: The Important Energy Transformer In a World of Sustainable Energy," *International Journal of Hydrogen Energy,* vol. 23, no. 8, pp. 661-666, August 1998.

[9] M. M. Rashid, K. A. M. Mohammad, H. Naseem and M. Danish, "Hydrogen Production by Water Electrolysis: A Review of Alkaline Water Electrolysis, PEM Water Electrolysis and High Temperature Water," *International Journal of Engineering and Advanced Technology,* vol. 4, no. 3, pp. 80-93, February 2015.

[10] Y. Yan, B. Y. Xia, B. Zhao and X. Wang, "A Review on Noble-Metal-Free Bifunctional Heterogeneous Catalysits for Overall Electrochemical Water Splitting," *Journal of Materials Chemistry A,* vol. 4, no. 45, pp. 17587-17603, 2016.

Chapter 3. Corrosion Behavior in SLM Nickel Alloy Inconel 718

3.1 Introduction

IN718 is a high-strength Ni-Cr based alloy developed for application in high stress environments. Though it is used extensively in the aerospace and energy industries, especially in turbine blades, aircraft and rocket engines, it has also found use in oil and gas production components where it requires high strength and stability against corrosion in chloride environments.

High strength in IN718 comes from the added niobium, titanium, and aluminum, which form intermetallic hardening precipitates γ'' (Ni$_3$Nb, centered tetragonal crystal) and γ' (Ni$_3$(Ti, Al), simple cubic crystal) respectively. Chromium and nickel crystallize together as austenitic γ phase (face centered cubic) and contribute to an excellent resistance to oxidation and corrosion at high temperatures [1].

Ideally, greater corrosion resistance is achieved when the material's microstructure is devoid of δ-phase and secondary precipitates along the grain boundaries [2]. However, it has been shown that in IN718, up to 7% volume fraction of δ-phase is not detrimental to corrosion resistance [3].

MC carbides present in the alloy may act as local cathodes, increasing pit susceptibility [4], and the presence of Laves phases is usually considered detrimental due to an overall reduction in material strength and ductility [5].

This research focused on characterizing the corrosion properties of IN718 fabricated through SLM in neutral, acidic, and alkaline NaCl environments before and after undergoing heat treatment. Tests were done on specimens as-printed, and after HIP. Results were compared to those obtained from traditionally manufactured wrought IN718.

3.2 Experimental

3.2.1 Materials and Heat Treatment

12.6 mm diameter IN718 rods fabricated by SLM were obtained from a vendor. The powder for the SLM process was supplied by Praxair Surface Technologies, USA (TruForm™ Metal

Powders) with a nominal composition of (wt%) Ni-19Cr-18Fe-5(Nb+Ta)-3Mo-1Ti-0.5Al. The 3D printing process was done on a SLM®-500 machine with a maximum laser power of 400 W. Component layer thickness was approximately 40 μm. Other processing parameters were not disclosed by the vendor. Samples that underwent HIP were processed using the optimal parameters mentioned in Chapter 1 (1180°C, 175 MPa 4 hrs soak). For comparison, traditionally wrought 12.54 mm diameter rods were procured from Carpenter Technology Corporation, USA. These samples were tested in acidic environments, as this was found to be the most corrosive. The composition of the wrought material was (in wt%) 52.65Ni-18.31Cr-18.2Fe-5.14(Nb+Ta)-2.88Mo-0.92Ti-0.51Al-0.04C-0.004B. The AM and Wrought IN718 samples had similar composition.

The heat treatment cycle consisted of a solution treatment (980°C for 1 hour, air-cool), followed by a two-step aging process (720°C for 8 hours, furnace-cool to 620°C at 55°C/hour, hold at 620°C for 8 hours, air-cool). Heat treated samples are designated (HT). Sample identification and heat treatment conditions are summarized in **Error! Reference source not f ound.**.

Table 3.2. Specimen identification and processing

Specimen ID	Processing condition
AS-AM or AS-AM (Received)	SLM printed without further conditioning
AS-AM (HT)	SLM printed + heat treated (solution annealing at 980 °C followed by two step aging treatment)
AM-HIP or AM-HIP (Received)	SLM printed and hot isostatically pressed
AM-HIP (HR)	SLM printed and hot isostatically pressed + heat treated (solution annealing at 980 °C followed by two step aging treatment)
Wrought Received	Wrought material in mill annealed condition – as received
Wrought (HT)	Wrought material heat treated (solution annealing at 980 °C followed by two step aging treatment)

3.2.2 Microstructure Characterization

Specimens were analyzed using X-ray diffraction (XRD). Microscopy was done using an optical microscope (OM) and scanning electron microscope (SEM) after immersion etching using waterless Kalling's Reagent (5 g $CuCl_2$, 100 ml HCl, and 100 ml ethanol). Vickers

hardness testing was carried out using a 500 g load with a minimum of ten readings per specimen. Grain size was determined through the linear intercept method following the ASTM standard E 112–13. The porosity volume fraction of each specimen was determined by measuring the apparent density of the according to ASTM standard B 962–08.

3.2.3 Electrochemical Tests

Samples with an area of 1.25 cm^2 $\pm$ 0.05 cm^2 were cut from stock and fabricated into working electrodes for experimentation by soldering insulated single-strand copper wire to the specimen sample then cold mounting in an acrylic resin to expose one side of the sample. Prior to each series of experiments, the surface of each tested specimen was treated by grinding with silicon carbide (SiC) papers consecutively up to 1200 grit before polishing using a 1 μm alumina slurry.

A standard three-electrode cell was used for experimentation, using a potassium chloride (KCl) saturated silver/silver chloride (Ag/AgCl) reference electrode (197 mV vs. standard hydrogen electrode) with a platinum (Pt) counter electrode. A Gamry Interface 1000 potentiostat was used to conduct the experiments. Electrochemical experiments were performed at room temperature in 3.5% sodium chloride (NaCl) solution at three pH levels; 6.25 (unadjusted NaCl solution), 1.25 (addition of 0.1 M hydrochloric acid (HCl)), and 12.25 (addition of 0.1 M sodium hydroxide (NaOH)). Allowable pH deviation was within 0.10 units of base level.

The open circuit potential (OCP) was observed for 1 hour before conducting linear polarization resistance tests over a range of OCP $\pm$ 25 mV using a scan rate of 5 mV/s. The samples were then subjected to electrochemical impedance spectroscopy (EIS) measurements at OCP by superimposing an AC amplitude of 10 mV. The frequency range was 0.01 Hz to 10 kHz. Finally, cyclic potientiodynamic polarization was performed, beginning at a potential approximately 100 mV below OCP at a scan rate of 0.5 mV/s. The forward scan continued until either until an apex potential of 1.6 V$_{Ag/AgCl}$ or an apex current density of 5 mA/cm^2 was reached, before reversing to initial OCP.

During the forward scan, the point at which the current begins to monotonically increase is defined as the transpassive potential (E_{TP}) where pitting may initiate. This point could either signify passivation breakdown or oxygen evolution.

To study pitting initiation behavior, the sample was repolished then conditioned at OCP. An EIS at 50 mV below the transpassive potential (E_{TP-50}) was conducted before potentiostatic testing at the same potential. When the current had increased by approximately 20 μm the test was halted and an additional EIS test was done. Finally, Mott-Schottky analysis was carried out, initializing at E_{TP-50} and ending at OCP, at 1000 Hz with a 50 mV potential step.

3.3 Results and Discussion

3.3.1 X-ray Diffraction and Microstructure Analysis

XRD tests were enacted using a Siemens Powder X-Ray Diffraction system using copper K-α radiation. Figure 3.4 displays the XRD profiles obtained after testing. Indexing was done using published lattice parameter values for IN718 [6] and the resulting peaks are consistent with previous work in analyzing IN718 [7, 8].

Both AS-AM samples showed predominant peaks in the (200) plane, indicating preferential growth in this orientation, as well as peaks occurring at 46.45° that could be associate with the δ-phase (Ni_3Nb with orthorhombic lattice structure) (211) plane. The intensity of this peak diminished after heat treatment, however there was little change in the primary (111), (200), and (220) peaks.

HIP specimens showed no indication of the presence of the δ-phase. HIP changed the preferential crystal orientation to the (111) plane and heat treatment changed it back to the (200) plane.
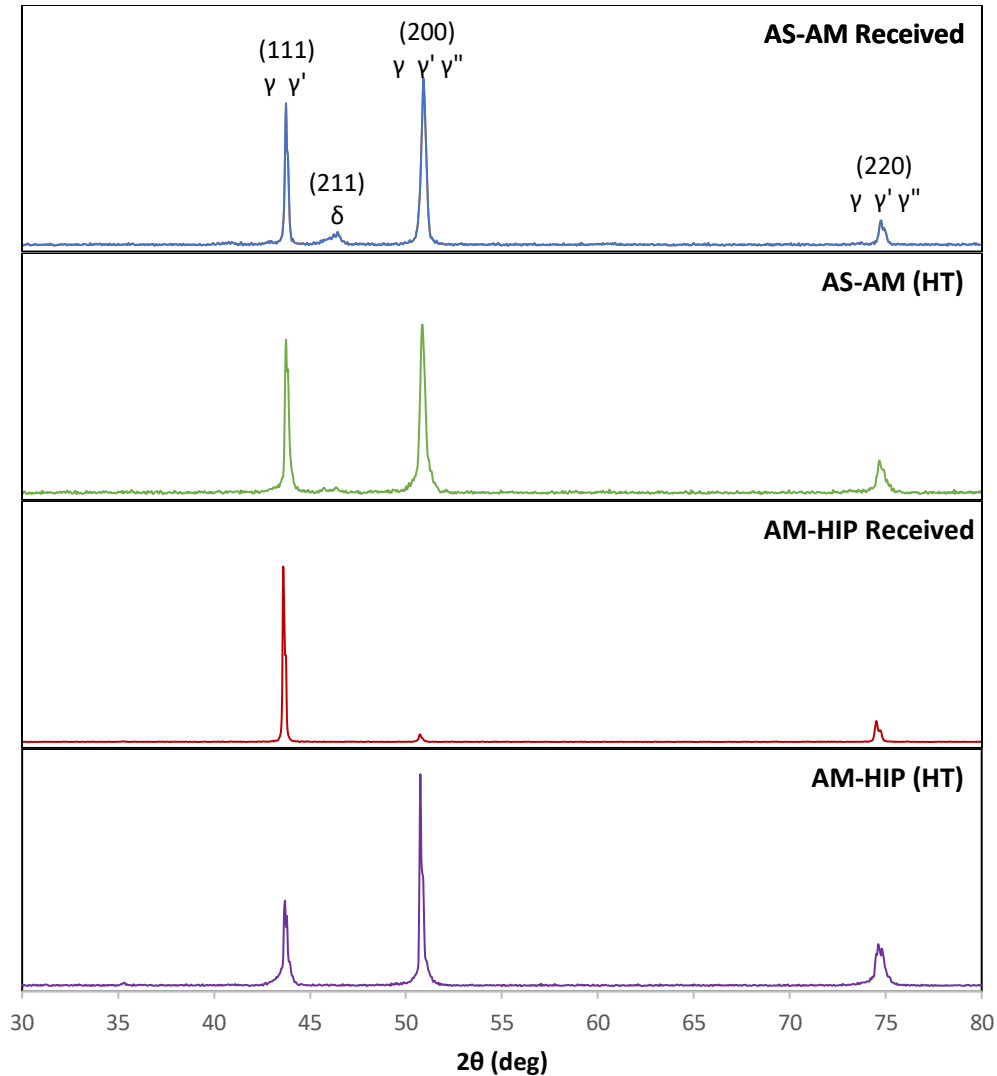
Figure 3.4. XRD patterns for SLM IN718 samples

Table **3.3** summarizes the microstructural conditions of the specimens. In all samples, overall hardness increased after heat treatment. Heat treatment did not significantly alter material grain size; however, grain size did increase after the HIP process. It should also be noted that the grain size number for AS-AM samples represents the elongated columnar grain structure. This is shown in Figure 3.5 (a) and (b).

The densities of as-received AS-AM and AM-HIP samples were measured using a Qualitest™ Densimeter 2SD-200L and the results were compared to published IN718 density values. The difference between measured and published data was attributed to porosity resulting from the

SLM process. AS-AM samples showed an overall porosity of nearly 3%, which was reduced in HIP samples to 0.67%

Table 3.3. Summary of hardness, grain size, and porosity of IN718 specimens

Specimen ID	Vickers hardness – range (average) (kgf/mm^2)	ASTM Grain size number (average diameter, μm)	Porosity, vol%
AS-AM Received	360 - 510 (420)	9.5 (13.3)	2.92 ± 0.2
AS-AM (HT)	419 - 535 (474)	10 (11.2)	-
AM-HIP Received	344 – 454 (408)	8 (22.5)	0.67 ± 0.06
AM-HIP (HT)	483 - 546 (516)	7.5 (26.7)	-
Wrought Received	339 – 409 (370)	9 (15.9)	-
Wrought (HT)	518 – 600 (562)	8.5 (18.9)	-

Figure 3.5(a)-(f) show the optical microscopy of both the SLM and wrought IN718 specimens before and after heat treatment. As stated previously, the AS-AM samples showed a columnar dendritic microstructure with present porosities. Pores are generally absent in HIP samples. Annealing twins are seen after heat treatment in the AM-HIP and wrought samples. In addition, an extensive network of grain boundary precipitates are seen on the heat treated wrought sample.
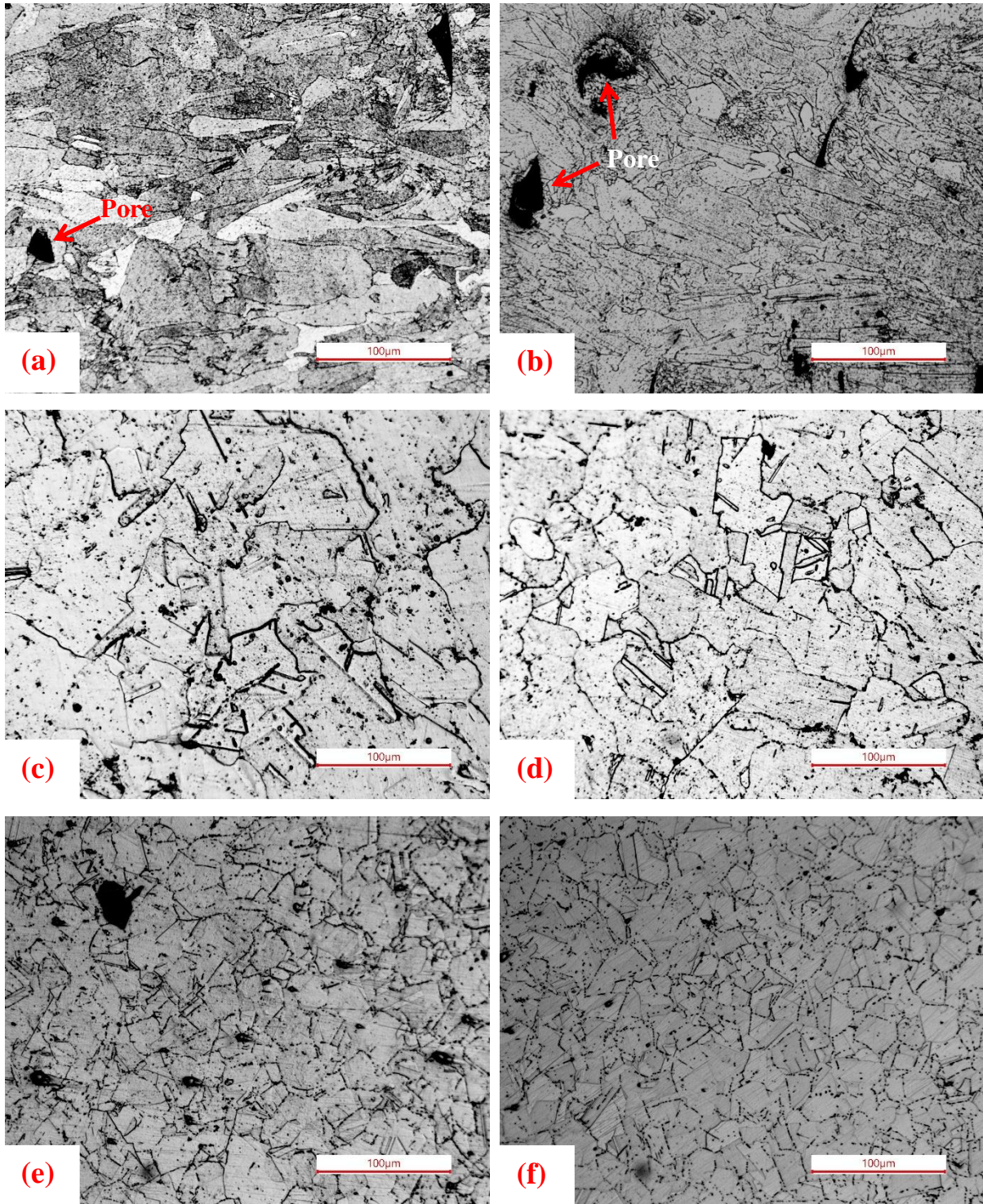
Figure 3.5. Optical microstructures of the IN718 specimens: (a) AS-AM Received, (b) AS-AM (HT), (c) AM-HIP Received, (d) AM-HIP (HT), (e) Wrought Received, (f) Wrought (HT)

Figure 3.6(a) and (b) show SEM images of AS-AM and AS-AM (HT) samples respectively and Figures 3.3(c) and (d) are zoomed-in images. AS-AM specimens reveal a network of δ-phase as well as Laves phase particles along the grain boundaries. At higher magnifications, other secondary phases (γ" and MC carbides) can be seen. MC carbides are precipitates consisting of a metal component attached to a carbon atom. Heat treatment greatly decreased the δ-phase concentration, though they were still present, as shown in 3.3(d). This could be due to the heat treatment (980°C) being lower than the solvus temperature of δ-phase (995°C), resulting in trace δ-phase needles.
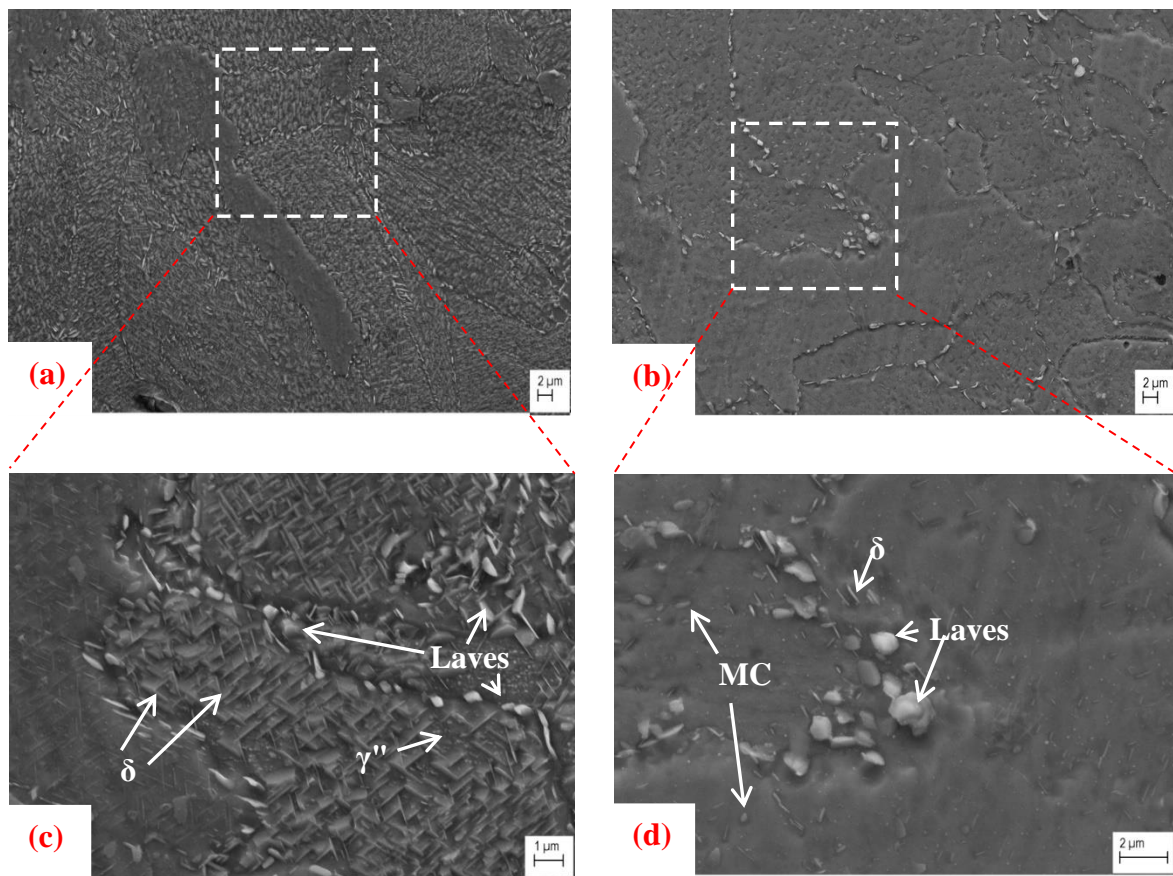
Figure 3.6. Secondary electron images (FE-SEM) of the etched microstructures of SLM IN718 specimens: (a) and (c) AS-AM Received, (b) and (d) AS-AM (HT)

Figure 3.7 (a) and (b) show the SEM images of the AM-HIP microstructures before and after heat treatment. HIP caused dissolution of the Laves and δ phases as well as a significant increase in formed precipitates at the grain boundaries after heat treatment.

Particles were identified using energy dispersive spectroscopy (EDS) analysis.

(a)

10 µm

(b)
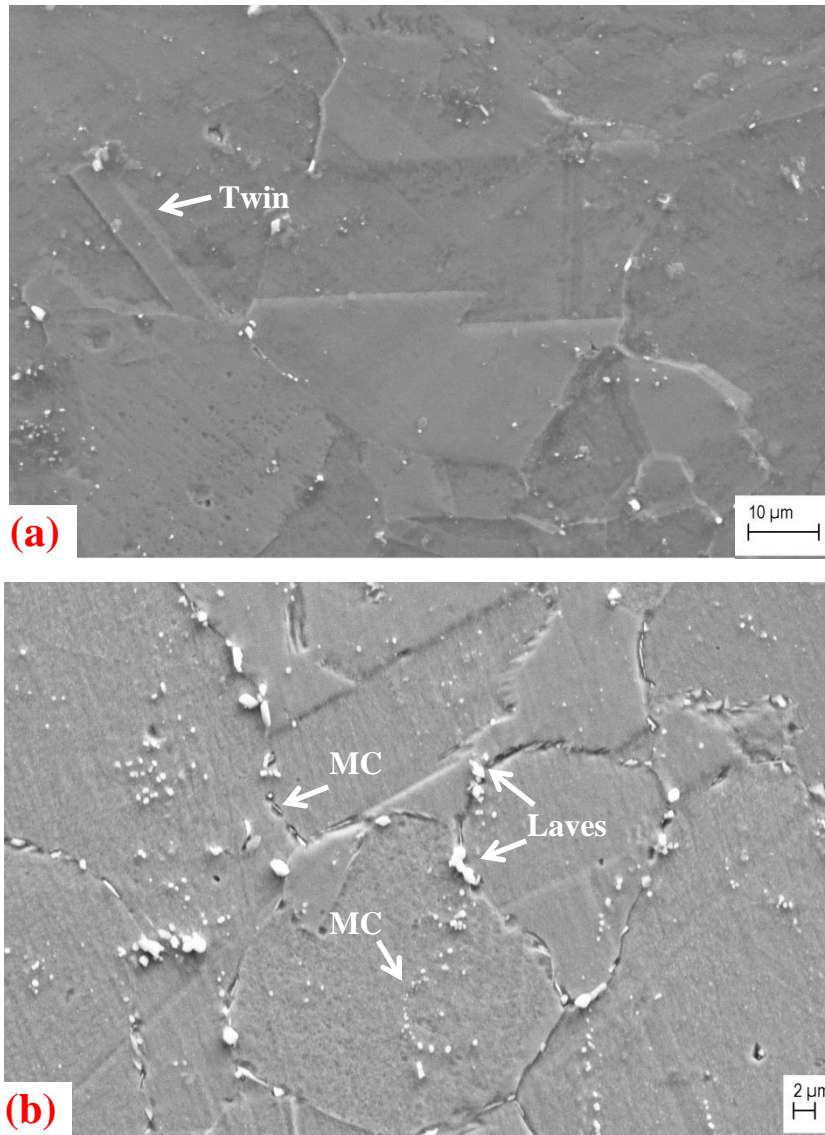
Figure 3.7. Secondary electron images (FE-SEM) of the etched microstructures of SLM IN718 specimens: (a) AM-HIP Received (b) AM-HIP (HT)

3.3.2 Open Circuit Potential

Figure 3.8 (a)-(d) show the OCP as a function of time for each of the IN718 samples. The OCP is determined by the mixed potentials of both the anodic (dissolution of metal material) and cathodic reactions. The cathodic reaction will consist primarily of oxygen reduction in high and neutral pH solutions, and mostly hydrogen evolution in low pH conditions.

In acidic conditions (pH=1.25) OCP decreased for both received and heat treated AS-AM samples, and increased in AM-HIP samples. This is shown in Figure 3.8(a). Decreasing OCP indicates unstable passive film formation in the AS-AM samples, while the increasing OCP in AM-HIP specimens show a thickening of the surface passive film that stabilized approximately 20 minutes into the experiment. Heat treated samples showed higher OCP than received samples.

In addition, Figure 3.8(d) shows the wrought samples in the same acidic conditions. Both samples show continuous increase in OCP, attributed to passive film thickening, and lower final OCP values than the SLM samples.

Samples tested in the neutral environment showed very little relative change in OCP, showing stable passive film through the duration of the experiment. As was the case in the acidic environment, HIP samples showed higher overall OCP.

Figure 3.8(d) shows the OCP profile in the alkaline solution. All tested samples show an increase of OCP with time, indicating possible thickening of the formed passive film.
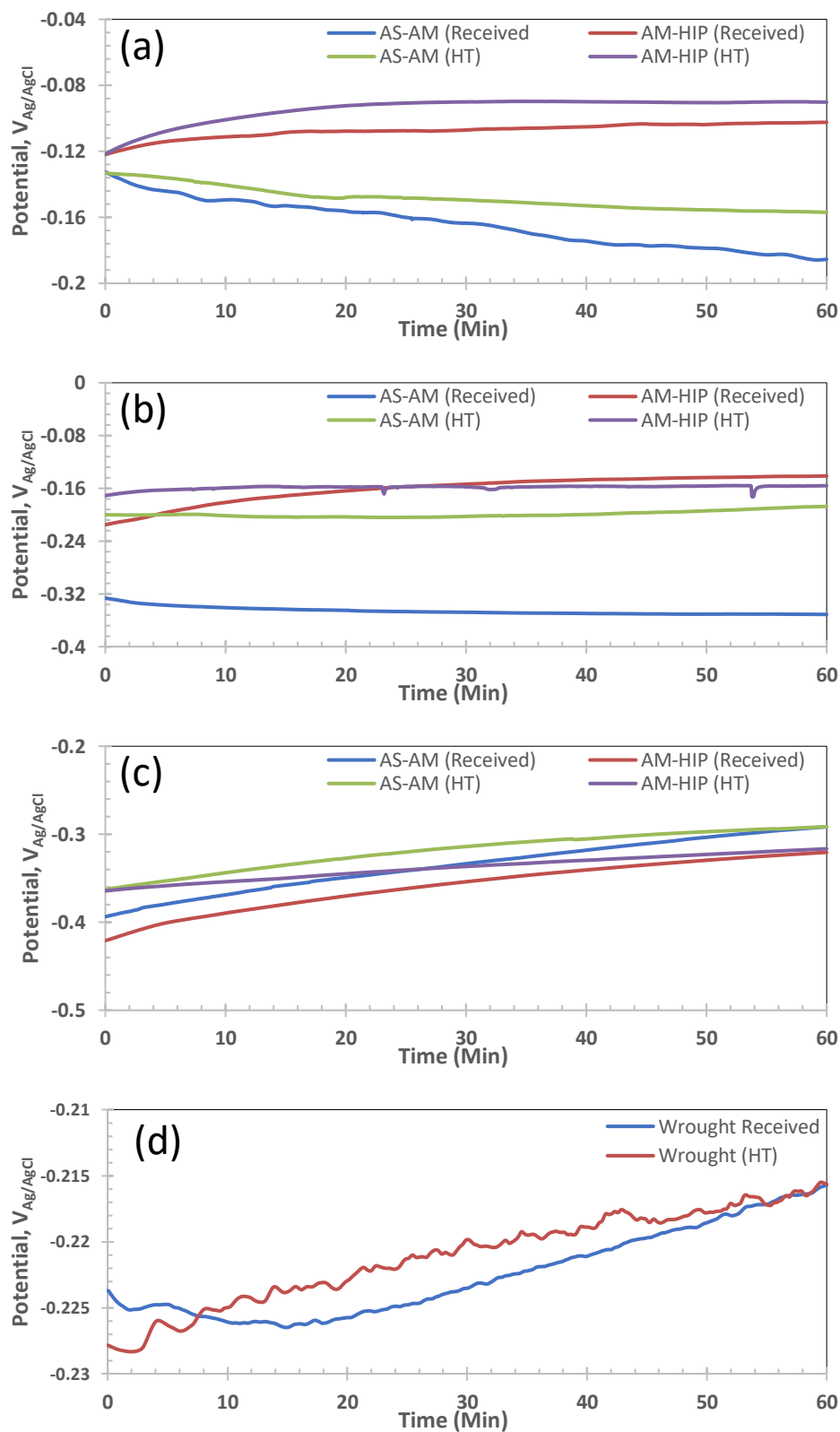
Figure 3.8. Open circuit potential plots for IN718 samples as a function of time in 3.5% NaCl solution with varying pH. (a) SLM samples, pH=1.25, (b) SLM samples, pH=6.25, (c) SLM samples, pH=12.25, (d) Wrought samples, pH=1.25

3.3.3 Linear Polarization Resistance

The Linear polarization resistance method consists of applying small potential variations to the working electrode above and below the determined OCP. The resulting slope show the difference in polarizing potential divided by the resulting current and is shown as ohms cm^2. Generally, a higher value indicates a greater resistance to corrosion.

Table 3.4 shows linear polarization results. AM-HIP samples showed higher polarization resistance in all pH conditions. AS-AM samples also showed comparatively high polarization resistance in neutral and alkaline solutions.

The tested wrought materials showed significantly lower polarization resistance in acidic conditions

Table 3.4. Linear polarization resistance results of IN718 specimens in 3.5% NaCl solution at different pH conditions

pH	Specimen ID	Linear Polarization Resistance (ohm cm^2)
1.25	AS-AM Received	5427.3
	AS-AM (HT)	7580.3
	AM-HIP Received	63682
	AM-HIP (HT)	47586
	Wrought Received	658
	Wrought (HT)	467
6.25	AS-AM Received	281180
	AS-AM (HT)	91058
	AM-HIP Received	222641
	AM-HIP (HT)	157219
12.25	AS-AM Received	162270
	AS-AM (HT)	55027
	AM-HIP Received	211407
	AM-HIP (HT)	93244

3.3.4 Electrochemical Impedance Spectroscopy at OCP

 Figure 3.9(a)-(d) shows the results of EIS at OCP. Wrought samples (shown in Figure 3.9(d)) showed the least impedance overall, indicating less resistance to corrosion. This corresponds with results obtained from the previously detailed linear polarization tests. In both the low and neutral pH environments, the order of impedance, from highest to lowest is shown as: AM-HIP, AM-HIP (HT), AS-AM (HT), AS-AM. This could indicate that Laves and δ-phases in the material present in AS-AM samples determine the general corrosion, as a higher concentration of Laves and δ-phases lower corrosion resistance. In alkaline solutions, the order of impedance was differed and is shown as: AM-HIP, AS-AM, AM-HIP (HT), AS-AM (HT).

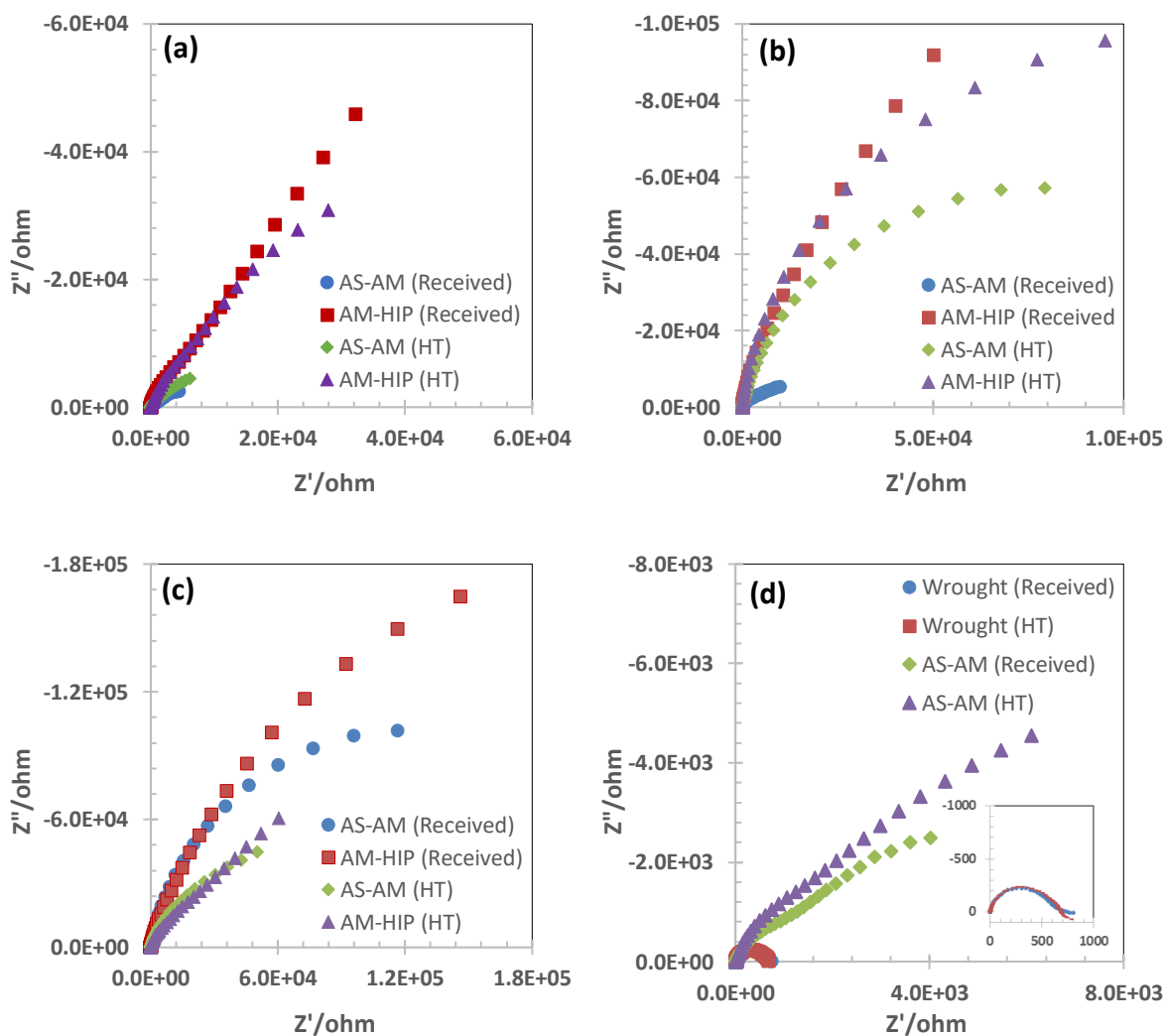**Figure 3.9.** Nyquist plots at OCP for IN718 samples in 3.5% NaCl solution with varying pH. (a) SLM samples, pH=1.25, (b) SLM samples, pH=6.25, (c) SLM samples, pH=12.25, (d) Wrought samples compared with AS-AM samples, pH=1.25

3.3.5 Cyclic Polarization

Cyclic polarization (CP) was used to evaluate each sample's susceptibility to pitting corrosion. Results are shown in Figure 3.10(a)-(c) (SLM samples) and Figure 3.11 (comparison of wrought with AS-AM samples). Table 3.5 summarizes the data taken from CP tests. Primary information taken from CP tests include the passivation current density i_P (minimum current density required to maintain passive film thickness), transpassive potential E_{TP} (potential at which the passive film begins dissolution or the take-off potential of the oxygen evolution reaction (OER)), and the pitting protection potential E_{PP} (threshold of pitting propagation; pits may not form or propagate below E_{PP}, however they may propagate if already initiated above E_{PP}). Good corrosion resistance is characterized by low i_P and high E_{TP} and E_{PP}.

Figure 3.10(a) shows the cyclic polarization plots of the SLM specimens in the acidic solution, and Figure 3.11 compares CP behavior of the wrought and SLM samples in the same environment. The wrought samples showed two orders of magnitude higher i_P than SLM samples, and the AM-HIP sample showed the lowest overall i_P. E_{TP} for these samples ranged from 0.925-1.04 $V_{Ag/AgCl}$. Considering that the redox potential of OER at pH 1.25 is 0.96 $V_{Ag/AgCl}$ and the high overpotential required to drive OER, it is likely that the observed transpassivity is due to passivation breakdown and not OER. This is further supported by the positive hysteresis (cross-over of the reverse scan at a potential more negative than the E_{TP}) seen on the CP plot.

The area of the hysteresis loop also gives some sign of the material's resistance to corrosion. Smaller hysteresis loops indicate faster pit repassivation, and therefore greater corrosion resistance. The absence of a hysteresis loop denotes a lack of pitting corrosion, though the material may still be subject to general corrosion.

CP results for the wrought material showed a very high passivation current density, but lacked a hysteresis loop.

CP results for SLM samples in neutral conditions are shown in Figure 3.10(b). The redox potential for OER in pH 6.25 is approximately 0.66 $V_{Ag/AgCl}$. The E_{TP} ranged 0.959-1.090. The high E_{TP} could indicate OER and the positive hysteresis observed could be the result of

passivation breakdown possibly assisted by OER. This could occur by the decomposition of the lattice oxygen of the passive film by the following reactions [9]:

$$4\ O^{2-} \rightarrow 4\ O^{1-} + 4e^- \qquad\qquad (3.1)$$

$$4\ O^{1-} \rightarrow 2\ (O_2)^{2-} \qquad\qquad (3.2)$$

$$2\ (O_2)^{2-} \rightarrow 2\ O^{2-} + O_2\uparrow \qquad\qquad (3.3)$$

The lattice oxygen evolution mechanism as suggested above involves formation of oxygen vacancies in the passive film and the defects could lead to localized corrosion of the material resulting in the hysteresis of the cyclic polarization. It is noted that the AM-HIP specimens showed higher transpassive potentials and pitting protection potentials than the specimens that had not undergone HIP.

Figure 3.10(c) shows the CP plots of the SLM specimens in the alkaline solutions. The redox potential of OER at pH=12.25 is 0.31 $V_{Ag/AgCl}$ and E_{TP} ranged 0.528-0.560 $V_{Ag/AgCl}$. All specimens showed negative hysteresis, indicating an absence of pitting. Transpassivity could be ascribed to general dissolution of the metal, without any localized corrosion.

The sharp increase in current in the samples above 0.6 $V_{Ag/AgCl}$ could be associated with the decomposition of lattice oxygen, as seen in Equation (3.1).
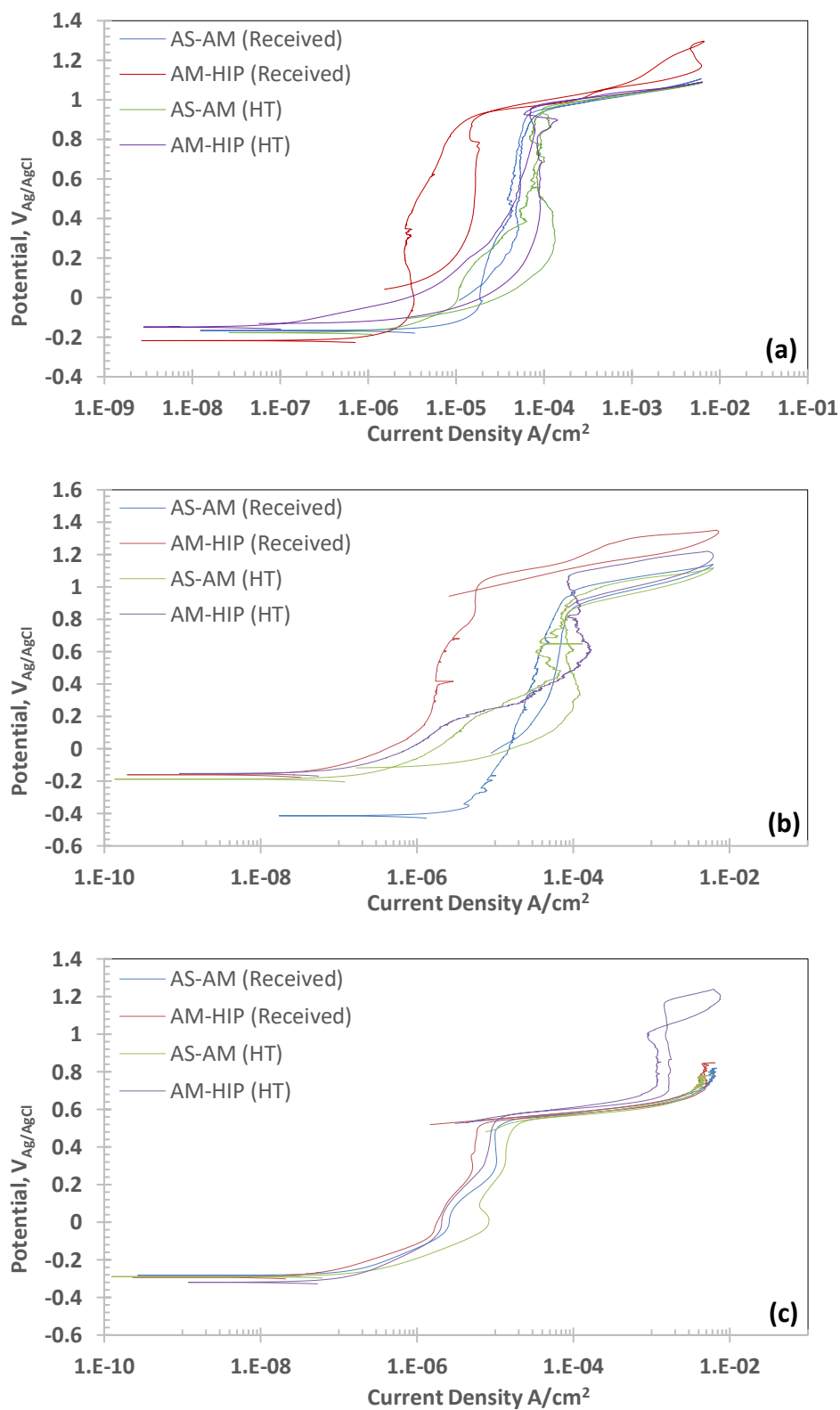
Figure 3.10. Cyclic polarization plots for SLM IN718 samples in 3.5% NaCl solution with varying pH. (a) pH=1.25, (b) pH=6.25, (c) pH=12.25
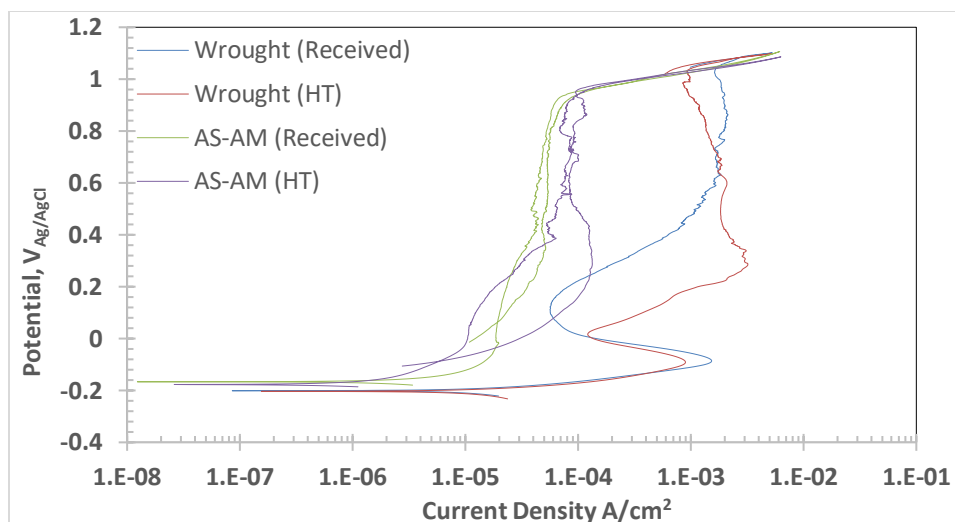
Figure 3.11. Cyclic polarization plots comparing wrought and SLM IN718 samples in 3.5% NaCl solution, pH=1.25

Table 3.5. Summary of the cyclic polarization measurements of IN718 specimens in 3.5% NaCl solution at different pH conditions.

pH	Specimen ID	OCP ($V_{Ag/AgCl}$)	Passivation current density, i_p (A/cm^2)	Transpassive potential, E_{TP} ($V_{Ag/AgCl}$)	Pitting protection potential, E_{PP} ($V_{Ag/AgCl}$)
1.25	AS-AM Received	-0.090	2.90E-05	0.937	-0.029
	AS-AM (HT)	-0.159	6.67E-05	0.962	0.082
	AM-HIP Received	-0.093	4.52E-06	0.925	0.047
	AM-HIP (HT)	-0.086	5.01E-05	0.960	-0.129
	Wrought Received	-0.216	1.76 E-03	1.04	-
	Wrought (HT)	-0.220	1.83 E -03	1.04	-
6.25	AS-AM Received	-0.333	3.28E-05	0.959	0.072
	AS-AM (HT)	-0.196	5.16E-05	0.944	-0.115
	AM-HIP Received	-0.143	3.88E-06	1.090	1.050
	AM-HIP (HT)	-0.155	8.03E-05	1.070	0.880
12.25	AS-AM Received	-0.329	2.02E-05	0.547	-
	AS-AM (HT)	-0.291	8.21E-06	0.539	-
	AM-HIP Received	-0.277	4.33E-06	0.528	-
	AM-HIP (HT)	-0.306	6.32E-06	0.560	-

3.3.6 Potentiostatic Polarization Tests

Potentiostatic polarization tests were used to assess passivation breakdown in the samples by monitoring changing current density over time with an applied potential of 50 mV under the found transpassive potential (E_{TP-50}). All samples experienced an initial current decay, revealing the formation of a passive layer on the surface of the material. A rising current indicated a breakdown in the passive film and probable pit initiation. When the current had risen by approximately 20 µA, the test was halted. Potentiostatic polarization plots are shown in Figure 3.12(a)-(d).

Figure 3.12(a) and (d) show the plots for samples tested in the acidic solution. Sample (AS-AM (HT) has the highest current density (indicating a less protective passive film) and fastest passivation breakdown. Both wrought samples showed a faster current decay. The AM-HIP sample showed lesser and stable current density after initial decay in all conditions, suggesting the formation of a thick impervious film.

Current decay in neutral and alkaline conditions generally followed the same trend observed in the acidic solution. In these conditions, the lack of a current rise in the AM-HIP samples may result from the applied potential being less than the pitting protection potential. It is interesting to note that in the alkaline solution, no hysteresis or pitting behavior was observed during cyclic polarization, however a current decay and subsequent rise was observed during potentiostatic conditioning.

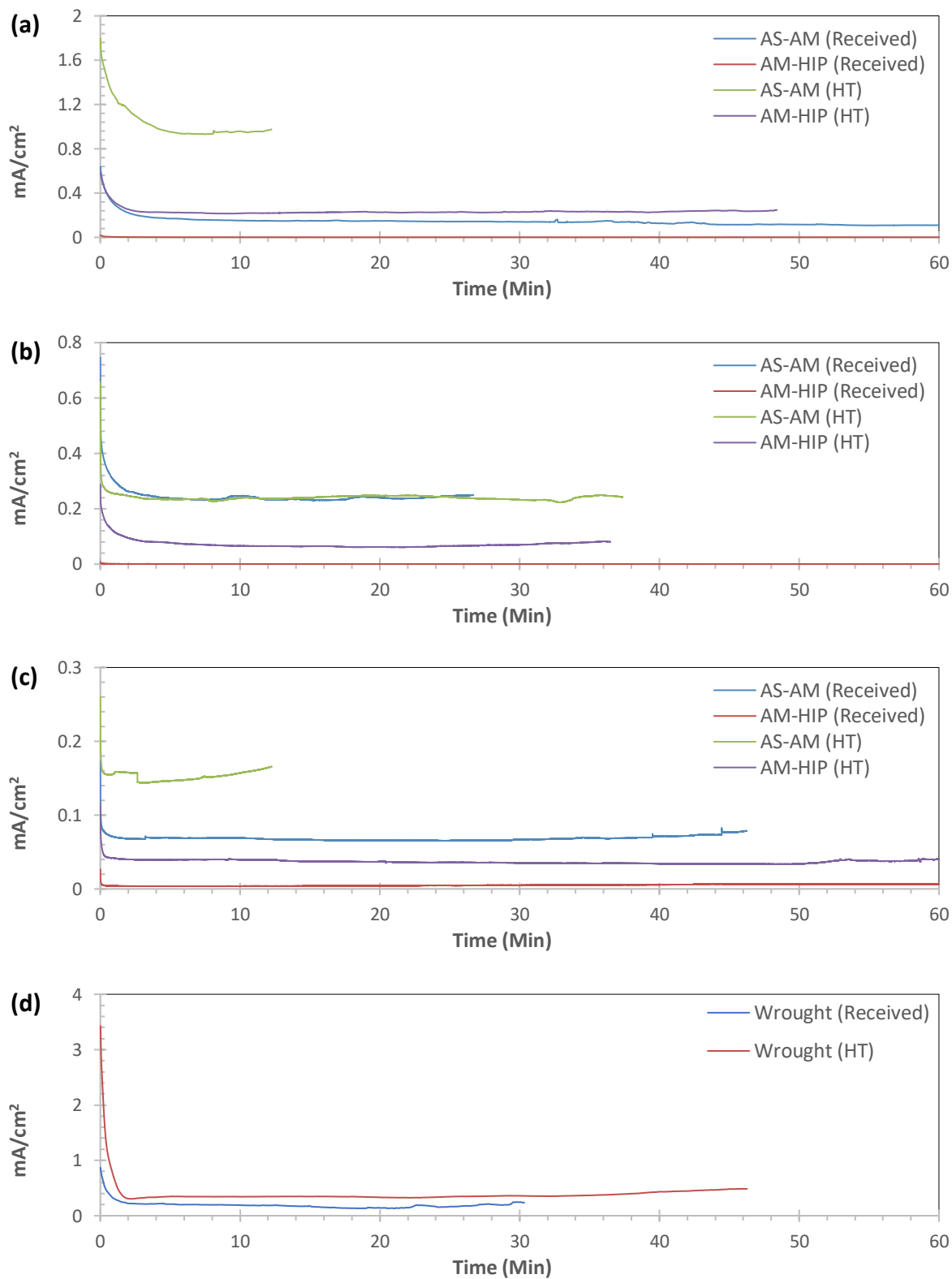**Figure 3.12.** Potentiostatic polarization plots for IN718 samples in 3.5% NaCl solution with varying pH. (a) SLM samples, pH=1.25, (b) SLM samples, pH=6.25, (c) SLM samples, pH=12.25, (d) Wrought samples, pH=1.25

3.3.7 Electrochemical Impedance Spectroscopy at $E_{TP\text{-}50}$

EIS was enacted before potentiostatic testing, and after the test was halted, at $E_{TP\text{-}50}$. The results were compared and the variance in the impedance behavior indicated the changing properties of the passive layer. Figures 3.10, 3.11, and 3.12 respectively show the obtained Nyquist plots for SLM IN718 for low, neutral, and high pH.

In the acidic solution (Figure 3.13(a)-(d)), impedance increased after potentiostatic testing for the AS-AM and AM-HIP specimens, indicating a thickening of the passive film over the duration of the test. The AS-AM (HT) sample showed the lowest overall impedance value, corresponding to the high current density shown during potentiostatic conditioning, and there was no significant change in impedance. Impedance decreased after potentiostatic testing for the AM-HIP (HT) sample.

Figure 3.14(a)-(d) exhibit the Nyquist plots for samples tested in the neutral environment. Impedance increased for the AM-HIP sample, indicating a stable passive condition. The decrease in impedance for both heat threated samples could be an indication of the detrimental effects of Laves phases in the specimens. There was no change in impedance for the AS-AM sample.

All samples tested in the alkaline environment (Figure 3.15(a)-(b)) showed a decrease in impedance after potentiostatic tests, suggesting occurrences of passivity breakdown.

Figure 3.13. Nyquist plots for IN718 in 3.5% NaCl solution before and after potentiostatic test. pH=1.25. (a) AS-AM (Received), (b) AM-HIP (Received), (c) AS-AM (HT), (d) AM-HIP (HT)

Figure 3.14. Nyquist plots for IN718 in 3.5% NaCl solution before and after potentiostatic test. pH=6.25. (a) AS-AM (Received), (b) AM-HIP (Received), (c) AS-AM (HT), (d) AM-HIP (HT)

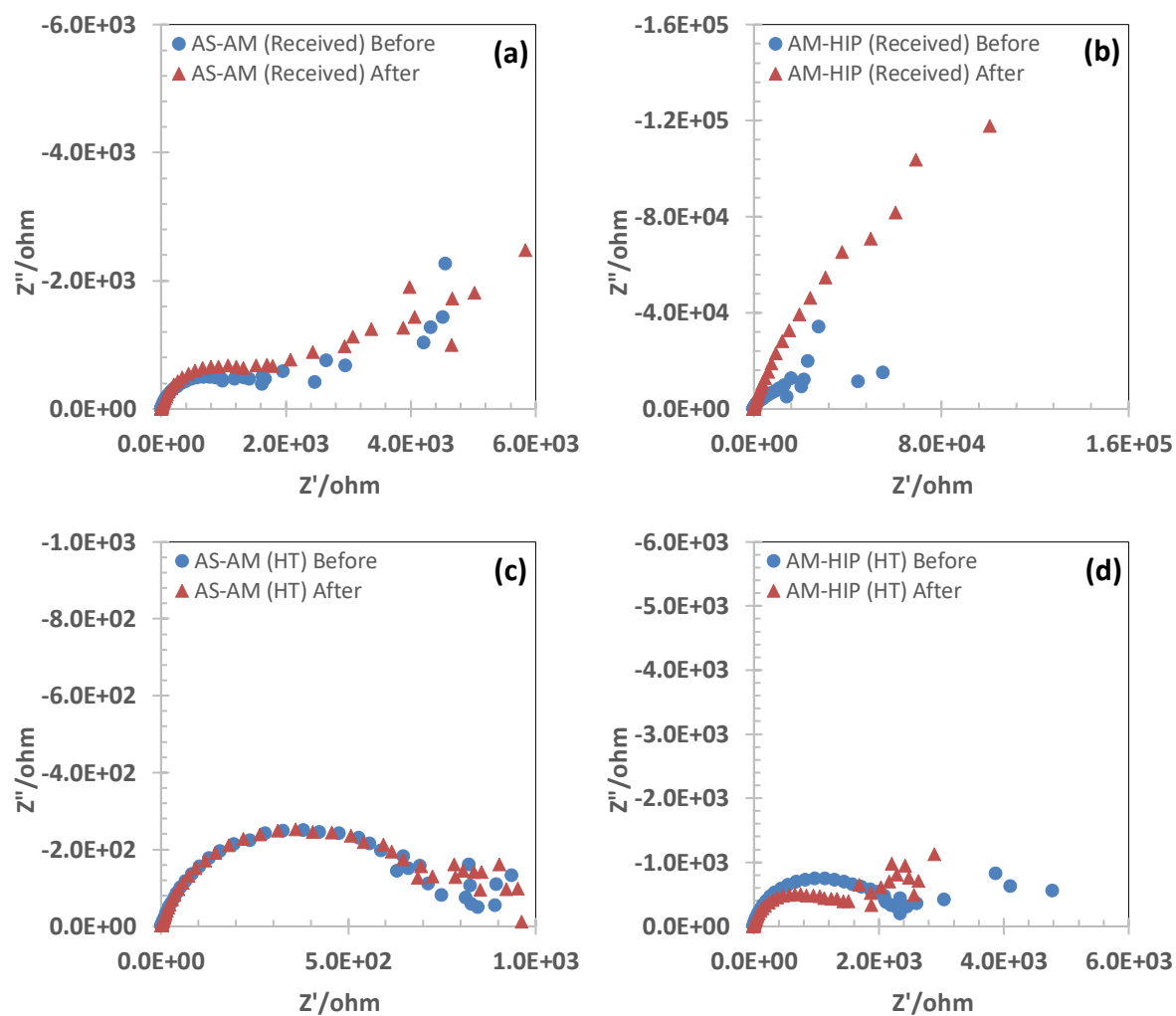**Figure 3.15.** Nyquist plots for IN718 in 3.5% NaCl solution before and after potentiostatic test. pH=12.25. (a) AS-AM (Received), (b) AM-HIP (Received), (c) AS-AM (HT), (d) AM-HIP (HT)
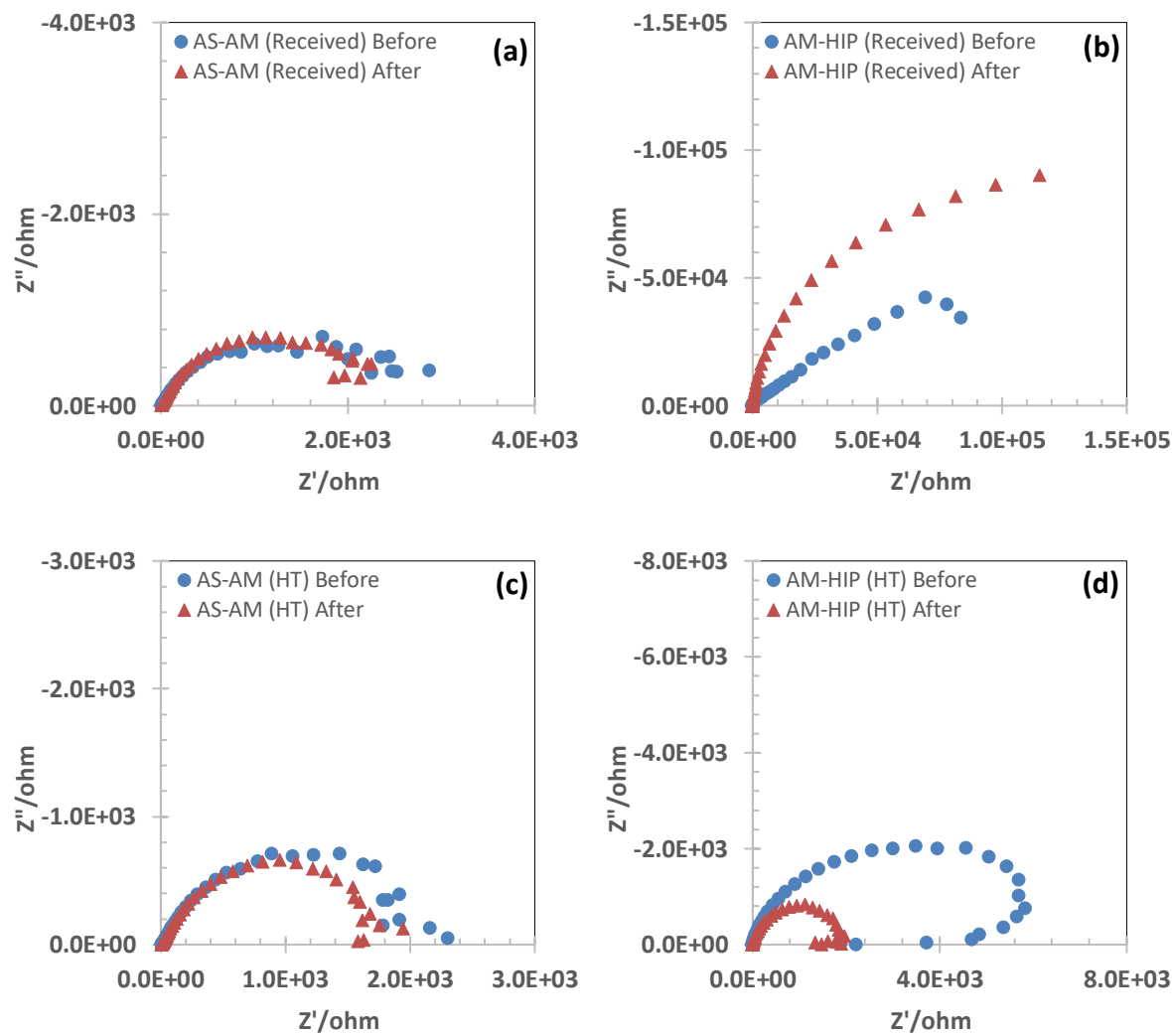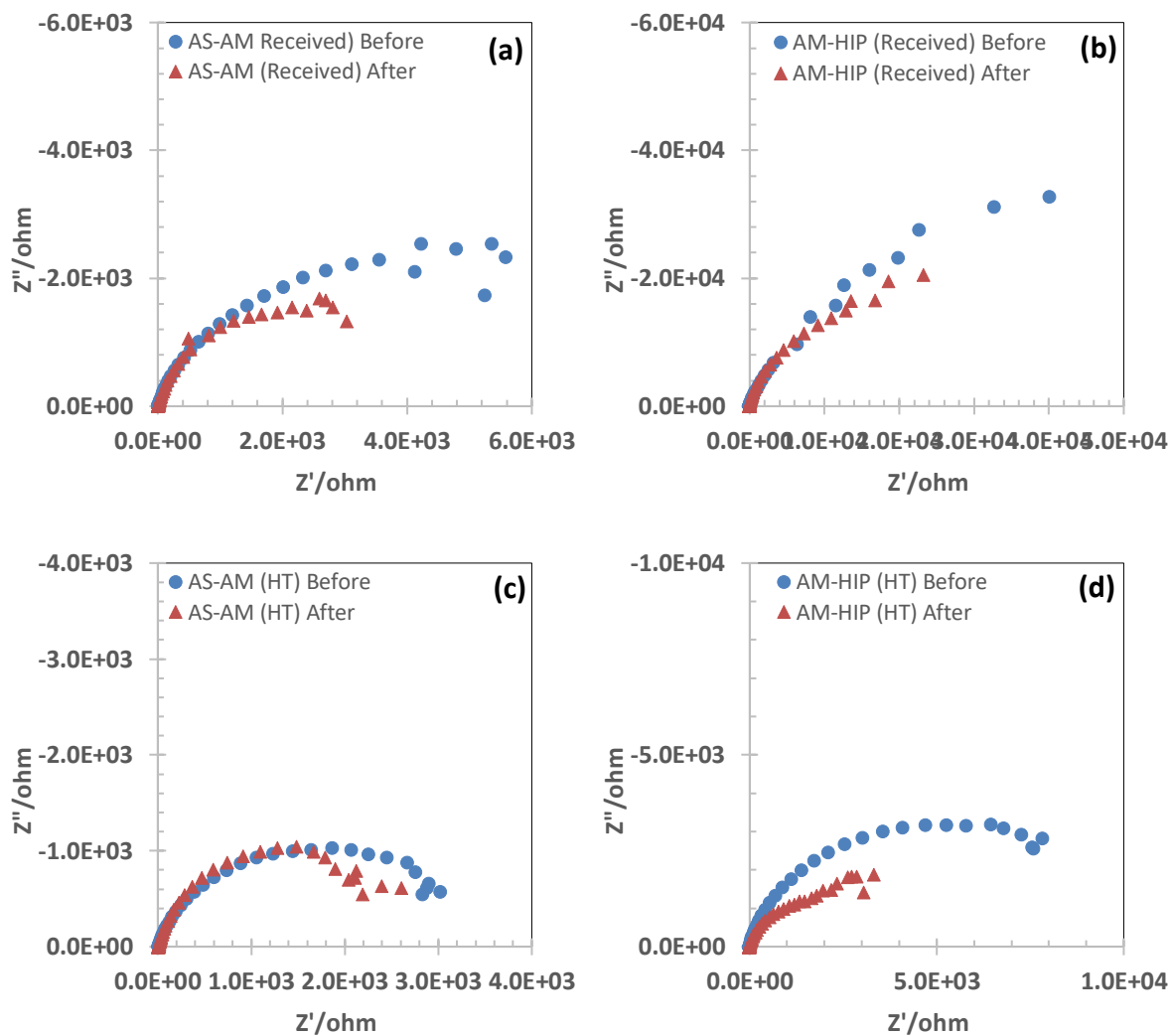
3.3.8 Mott-Schottky Tests

The SLM and wrought samples underwent Mott-Schottky analysis after the potentiostatic testing. The resulting plots are shown in Figure 3.16(a)-(d). The charge carrier density calculated from the slope of the Mott-Schottky plots and the determined flat band potentials are summarized in Tables 3.5, 3.6, and 3.7. In general, an increase in charge carrier density leads to higher conductivity or lower impedance, and therefore a lower resistance to corrosion. The formula for calculating charge carrier density is given as:

$$\text{Charge Carrier Density} = \frac{2}{q \varepsilon S k} \tag{3.4}$$

where q is the elementary charge (1.6 X 10^{-19} C), ε is absolute permittivity (8.854 X 10^{-14} F/cm), S is measured Mott-Schottky plot slope, and k is the material dielectric constant (13).

The Mott-Schottky plots showed both positive and negative slopes depending on the applied potential and pH conditions. A positive slope indicates an n-type semiconductor on the material's surface, and a negative slope indicates a p-type semiconductor. Prescence of both types could suggest a dual-layered passive film. Another possible explanation for the switch form n-type semiconductivity to p-type semiconductivity at high anodic potentials could be due to the formation of an inversion layer enriched with holes resulting from very large band bending caused by anodic polarization, or by the formation of cation vacancies in the passive film due to oxidation of transition metal ions to higher valence states.

Predominantly n-type semiconducting behavior was seen in the acidic solutions, both n and p-type semiconductivity were observed in the neutral solution, and only p-type semiconductivity was seen in the alkaline solution. Both NiO and Cr_2O_3 show p-type semiconductivity, so these are likely present in the corresponding passive films. Other alloying elements may also be included. In n-type semiconductors, a spinel type composition is expected.
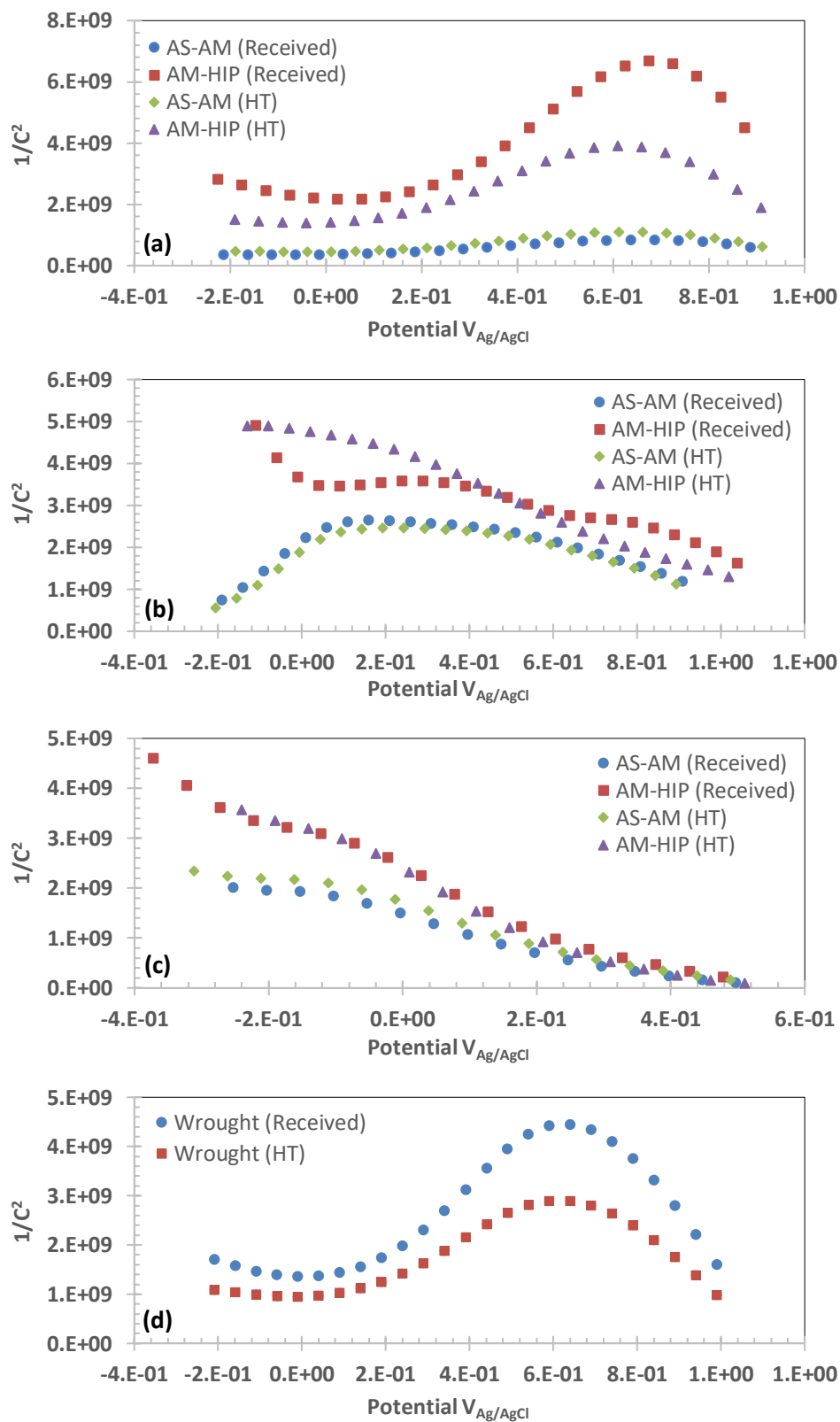
Figure 3.16. Mott-Schottky plots for IN718 samples in 3.5% NaCl solution with varying pH. (a) SLM samples, pH=1.25, (b) SLM samples, pH=6.25, (c) SLM samples, pH=12.25, (d) Wrought samples, pH=1.25

Table 3.6. Data for Mott-Schottky test for IN718 after potentiostatic test in 3.5% NaCl solution, pH=1.25

pH=1.25		Positive Slope				Negative Slope	
Specimen	Slope	Charge Carrier Density (cm^{-3})	Flat Band Potential		Slope	Charge Carrier Density (cm^{-3})	Flat Band Potential
AS-AM Received	1.05E+09	1.03E+22	-0.225		-	-	-
AS-AM (HT)	1.48E+09	7.35E+21	-0.185		-	-	-
AM-HIP Received	1.11E+10	9.79E+20	0.02		-	-	-
AM-HIP (HT)	6.47E+09	1.68E+21	-0.065		-	-	-
Wrought Received	8.23E+09	1.32E+21	0.09		-1.03E+10	-1.06E+21	1.15
Wrought (HT)	4.92E+09	2.21E+21	-0.05		-7.12E+09	-1.52E+21	1.14

Table 3.7. Data for Mott-Schottky test for IN718 after potentiostatic test in 3.5% NaCl solution pH=6.25

pH=6.25		Negative Slope				Positive Slope	
Specimen	Slope	Charge Carrier Density (cm^{-3})	Flat Band Potential		Slope	Charge Carrier Density (cm^{-3})	Flat Band Potential
AS-AM Received	-3.01E+09	-3.60E+21	0.32		8.18E+09	1.33E+21	-0.27
AS-AM (HT)	-3.10E+09	-3.50E+21	1.28		7.87E+09	1.38E+21	-0.25
AM-HIP Received	-3.13E+09	-3.47E+21	1.49		-	-	-
AM-HIP (HT)	-4.52E+09	-2.40E+21	1.19		-	-	-

Table 3.8. Data for Mott-Schottky test for IN718 after potentiostatic test in 3.5% NaCl solution pH=12.25

pH=12.25	Negative Slope		
Specimen	Slope	Charge Carrier Density (cm^{-3})	Flat Band Potential
AS-AM Received	-4.09E+09	-2.65E+21	0.36
AS-AM (HT)	-4.79E+09	-2.27E+21	0.36
AM-HIP Received	-7.24E+09	-1.50E+21	0.339
AM-HIP (HT)	-1.16E+09	-9.40E+21	0.31

3.4 Conclusions

Both received and heat treated AS-AM samples were relatively porous and revealed a fine columnar microstructure. Porosity greatly decreased and grains became more uniform after HIP.

Received samples showed a uniform distribution of δ-phase needles, Laves phases as interdendrites, and unresolved γ' and γ'' precipitates. Though these microstructures may be desirable for mechanical properties, they can be detrimental to corrosion resistance. In particular, the Laves and δ-phases may result in a lower Cr_2O_3 content and higher NiO content in the passive film, rendering it less effective in corrosion resistance [10]. The pores present in both received and heat treated AS-AM may also adversely affect material repassivation.

AM-HIP samples showed higher corrosion resistance in all pH conditions and corrosion resistance decreased after heat treatment in all samples.

SLM samples showed greater corrosion resistance than wrought samples in the tested acidic environment.

Overall, there is strong indication that Laves phases play a significant role in determining the corrosion behavior of IN718.

Through electrochemical testing, it was determined that AM-HIP samples generally showed higher corrosion resistance that could be correlated to the decrease in porosity level after HIP, and the absence of the dendritic structure.

Transpassivity observed during cyclic polarization could be attributed to OER induced by lattice oxygen decomposition in the passive film.

Positive hysteresis was observed in tested SLM samples during cyclic polarization in acidic and neutral solutions, indicating the initiation of localized corrosion. SLM samples in alkaline solutions and wrought samples in acidic solutions showed negative hysteresis during cyclic polarization, indicating a lack of passivity breakdown.

3.5 References

[1] A. Thomas, M. El-Wahabi, J. M. Cabrera and J. M. Prado, "High Temperature Deformation of Inconel 718," *Journal of Materials Processing Technology,* vol. 177, no. 1-3, pp. 469-472, 2006.

[2] *API SPEC 6A718-2004, Specification of Nickel Base Alloy 718 (UNS N07718) for Oil and Gas Drilling and Production Equipment,* American Petroleum Institute, 2004.

[3] L. Valle, A. Santana, M. Rezende, J. Dille, O. Mattos and L. de Almeida, "The Influence of Corrosion Behavior of Nickel-Based Alloy 718," *Journal of Alloys and Compounds,* vol. 809, p. 151781, November 2019.

[4] X. Wei and W. J. Zheng, "Effect of Carbides on Sensitivity of Pitting Corrosion in Inconel 718 Alloy," *Anti-Corrosion Methods and Materials,* vol. 67, no. 2, pp. 158-165, February 2020.

[5] J. J. Schirra, R. H. Caless and R. W. Hatala, "The Effect of Laves Phase on the Mechanical Properties of Wrought and Cast+HIP Inconel 718," in *Superalloys 718, 625, and Various Derivatives*, E. A. Loria, Ed., The Minerals, Metals & Materials Society, 1991, pp. 375-388.

[6] R. M. Nunes, D. Pereira, T. Clarke and T. K. Hirsch, "Delta Phase Characterization in Inconel 718 Alloys Through X-ray Diffraction," *ISIJ International,* vol. 55, no. 11, pp. 2450-2454, 2015.

[7] Q. Jia and D. Gu, "Selective Laser Melting Additive Manufacturing of Inconel 718: Superalloy Parts: Densification, Microstructure and Properties," *Journal of Alloys and Compounds,* vol. 585, pp. 713-721, 2014.

[8] G. H. Cao, T. Y. Sun, C. H. Wang, X. Li, M. Liu, Z. X. Zhang, P. F. Hu, A. M. Russell, R. Schneider, D. Gerthsen, Z. J. Zhou, C. P. Li and G. F. Chen, "Investigations of γ', γ'' and δ Precipitates in Heat-Treated Inconel 718 Alloy Fabricated by Selective Laser Melting," *Materials Characterization,* vol. 136, pp. 398-406, February 2018.

[9] K. Luo, M. Roberts, N. Guerrini, N. Tapia-Ruiz, R. Hao, F. Massel, D. M. Pickup, S. Ramos, Y.-S. Liu, J. Guo, A. V. Chadwick, L. C. Duda and P. G. Bruce, "Anion Redox Chemistry in the Cobalt Free 3d Transition Metal Oxide Intercalation Electrode Li[Li0.2Ni0.2Mn0.6]O2," *Journal of the American Chemical Society,* vol. 138, no. 35, pp. 11211-111218, 2016.

[10] L. Zhang and O. A. Ojo, "Corrosion Behavior of Wire Arc Additive Manufactured Inconel 718 Super Alloy," *Journal of Alloys nad Compounds,* vol. 829, p. 154455, July 2020.

Chapter 4. Electrocatalytic Feasibility of Inconel 718 Electrodes

4.1 Introduction

A key topic of interest in the development of reliable, clean, and renewable energy alternatives. concerns the production and exploitation of hydrogen for industrial fuel, and in the operation of hydrogen-based batteries and fuel cells.

Water splitting (electrolysis) is a common method of hydrogen production and consists of an electric current that is passed through water (H_2O) to fundamentally break the molecule down into hydrogen and oxygen. HER is the cathodic half-reaction and OER is the limiting corresponding anodic half-reaction.

Alkaline water electrolysis is the prevalent method used. Two water molecules (H_2O) are reduced to one hydrogen molecule (H_2) and two hydroxyl ions (OH^-) at the cathode (HER process). The hydrogen escapes as a gas while the hydroxyl ions migrate to the anode and are discharged as one molecule of water and ½ molecule of oxygen (OER process). The oxygen recombines and escapes as a gas. [1, 2]

The metal electrocatalyst used is an important factor in the efficiency of the electrochemical reaction processes. An ideal electrocatalyst will maximize overall process efficiency and generally include pure or alloyed noble metals, such as platinum (Pt), as well as ruthenium (Ru), and palladium (Pd) due to the high overpotential required. However high cost and scarcity prevent these metals from being practical choices in most circumstances, therefore there has been much research in finding low-cost alternative nonprecious alloys to act as an efficient electrocatalyst [3].

Nickel-based alloys have found considerable favor as a cost-effective electrocatalyst material due to high electrical conductivity and thermal stability, as well as excellent resistance to corrosion [4]. Nickel has been utilized as a key component in nickel-metal hydride (NiMH) batteries [5] and in more advanced long-use nickel-hydrogen batteries used extensively in air and space craft [6]. Nickel and nickel foam have also been used as primary electrocatalysts in various electrolysis applications [4, 7]

This study examined the electrocatalytic feasibility of IN718 fabricated through SLM in neutral, acidic, and alkaline NaCl environments before and after heat treatment. Tests were done on samples as-printed, and those that had undergone HIP. Results were compared to those obtained from traditionally manufactured wrought IN718.

4.2 Experimental

4.2.1 Materials and Heat Treatment

SLM and wrought IN718 samples were obtained from the same stock used in the corrosion experiments described in Chapter 3. Samples included specimens as-printed (designated AS-AM) and those that had undergone HIP (AM-HIP). Tests were completed on samples before and after heat treatment. Heat treatment consisted of a solution treatment (980°C for 1 hour, air-cool), followed by a two-step aging process (720°C for 8 hours, furnace-cool to 620°C at 55°C/hour, hold at 620°C for 8 hours, air-cool). Wrought samples were only tested in alkaline solutions, as that was shown to be the most effective electrocatalytic environment. Sample identification and heat treatment conditions are summarized in Table 4.9.

Table 4.9. Specimen identification and processing

Specimen ID	Processing condition
AS-AM or AS-AM (Received)	SLM printed without further conditioning
AS-AM (HT)	SLM printed + heat treated (solution annealing at 980 ℃ followed by two step aging treatment)
AM-HIP or AM-HIP (Received)	SLM printed and hot isostatically pressed
AM-HIP (HR)	SLM printed and hot isostatically pressed + heat treated (solution annealing at 980 ℃ followed by two step aging treatment)
Wrought Received	Wrought material in mill annealed condition – as received
Wrought (HT)	Wrought material heat treated (solution annealing at 980 ℃ followed by two step aging treatment)

4.2.2 Electrochemical Tests

The samples were prepared and tested in the same manner described in Chapter 3 and electrochemical experiments were carried out at room temperature using the described three-electrode cell in 3.5% NaCl solution (simulating natural seawater). Samples were tested at

three pH levels; 6.25 (unadjusted NaCl solution), 1.25 (addition of 0.1 M HCl), and 12.25 (addition of 0.1 M NaOH). Allowable pH deviation was within 0.10 units of base level.

Primary experiments consisted of monitoring OCP for 30 minutes to establish a base potential, followed by potentiodynamic polarization to -1 V vs OCP with a scan rate of 0.5 mV/s.

Because industrial water splitting is generally enacted in alkaline solutions, additional 24-hour galvanostatic tests were performed at high pH (pH=12.90) focusing on hydrogen and oxygen evolution. Alkaline environments are overall much less corrosive to the electrocatalyst, and are less expensive to maintain [8]. This allows for more efficient use of nonprecious electrocatalysts while allowing for a faster reaction [2].

To evaluate hydrogen evolution, the applied current density for galvanostatic testing was -10 mA/cm^2. For oxygen evolution, +10 mA/cm^2 was applied.

At the conclusion of each 24-hour galvanostatic test, MS analysis was performed. For hydrogen evolution tests, MS initiated at OCP and ended at the final potential determined by the galvanostatic test and for oxygen evolution, MS initiated at the found final potential and ended at OCP.

4.3 Results and Discussion

4.3.1 Potentiodynamic Polarization

Figure 4.17(a)-(d) show the resulting plots of potentiodynamic testing on the IN718 samples at three pH levels. These results are summarized in Tables 4.2 and 4.3 for HER and ORR respectively. Exchange current density (i_0) is defined as the rate of oxidation or reduction at the equilibrium electrode and was found where the plotted Tafel slope intersected the calculated redox potential. Generally, a higher i_0 corresponds to a faster reaction. The redox potential (E_{redox}) was determined using the following equations:

$$0 - (0.059 \bullet pH) - 0.2 \qquad V_{Ag/AgCl} \text{ for Hydrogen Evolution} \qquad (4.1)$$

$$1.23 - (0.059 \bullet pH) - 0.2 \qquad V_{Ag/AgCl} \text{ for Oxygen Reduction} \qquad (4.2)$$

In general, for HER, samples subjected to the most acidic environment exhibited the highest i_0 value indicating greater overall H_2 production. Sample AM-HIP (HT) showed the greatest exchange current density of 0.493 mA/cm^2. Experiments conducted in neutral pH conditions showed the least i_0.

The Tafel slope is used to determine overpotential increase needed to increase the reaction rate. Therefore, a lower Tafel slope is desired. Tafel slopes for HER remained generally consistent across all tested samples in each of the neutral and alkaline environment experiment sets. The heat treated wrought sample tested in the alkaline environment proved to be an outlier, with a much steeper slope than the corresponding additively manufactured samples. The lowest Tafel slopes were seen in samples tested in the alkaline solution.

There is greater deviation between individual samples in the acidic environment with as-received samples showing steeper slopes than heat-treated samples.

Oxygen reduction was negligible in the observed acidic environment. And in all samples at each pH level, i_0 increased after heat treatment, indicating a slower reaction. Samples tested under alkaline conditions generally had a greater i_0, with the exception of AM-HIP samples showing the lowest observed i_0 for oxygen reduction, at 2.89×10^{-9} mA/cm^2. As with HER, there was little deviation between Tafel slopes at each pH level.
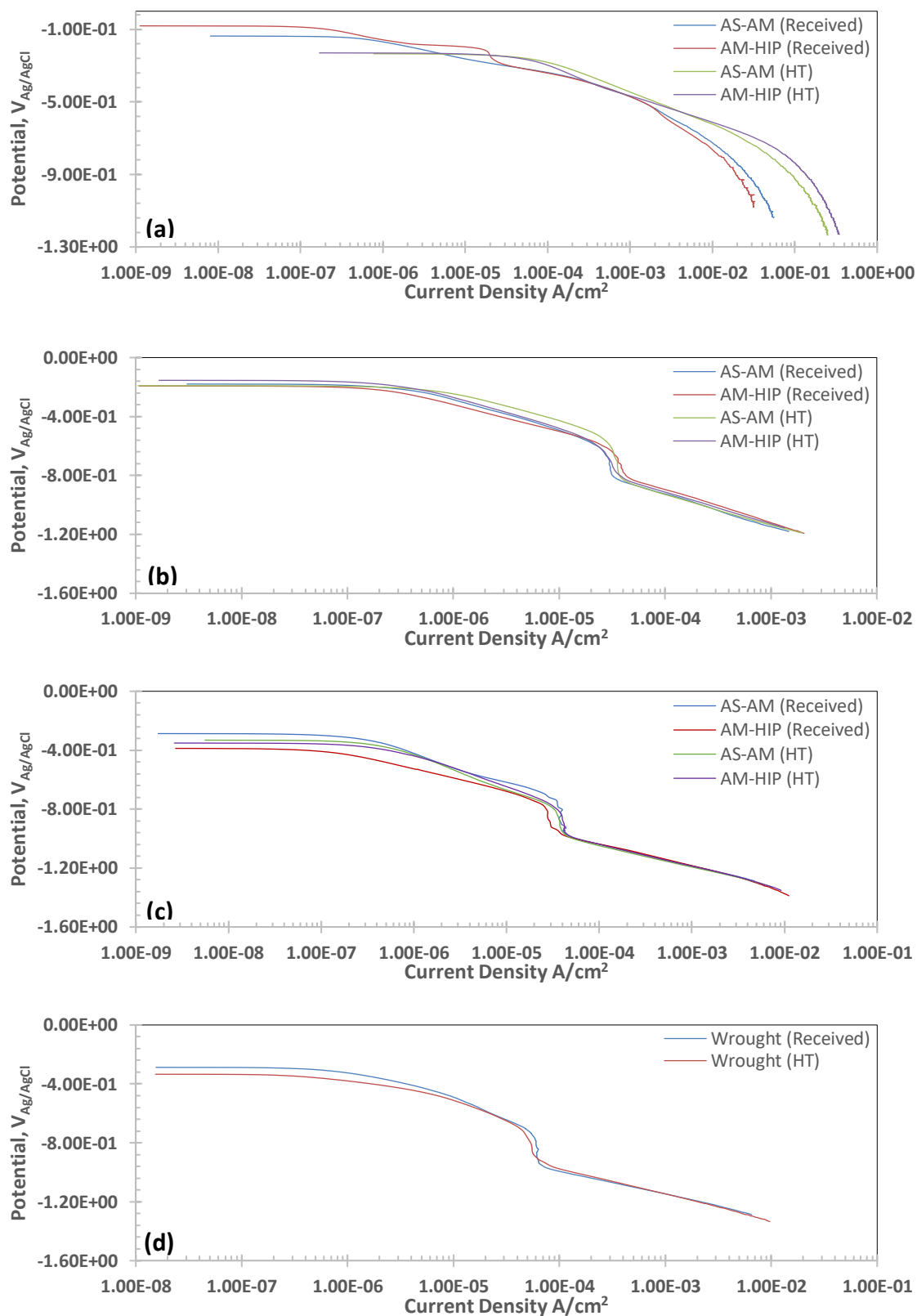
Figure 4.17. Potentiodynamic polarization plots for IN718 samples in 3.5% NaCl solution with varying pH. (a) SLM samples, pH=1.25, (b) SLM samples, pH=6.25, (c) SLM samples, pH=12.25, (d) Wrought samples, pH=12.25

Table 4.10. Summary of HER Behavior of IN718 in 3.5% NaCl solution with varying pH

pH	Specimen	i_0 (mA/cm^2)	Tafel Slope (V/Dec)
1.25	AS-AM Received	1.57×10^{-1}	-0.236
	AS-AM (HT)	1.05×10^{-1}	-0.176
	AM-HIP Received	2.88×10^{-1}	-0.313
	AM-HIP (HT)	4.93×10^{-1}	-0.144
6.25	AS-AM Received	3.14×10^{-3}	-0.231
	AS-AM (HT)	1.83×10^{-3}	-0.207
	AM-HIP Received	3.52×10^{-3}	-0.228
	AM-HIP (HT)	2.31×10^{-3}	-0.209
12.25	AS-AM Received	1.45×10^{-2}	-0.140
	AS-AM (HT)	1.38×10^{-2}	-0.140
	AM-HIP Received	2.37×10^{-2}	-0.150
	AM-HIP (HT)	1.72×10^{-2}	-0.150
	Wrought Received	3.66×10^{-2}	-0.158
	Wrought (HT)	4.99×10^{-2}	-0.175

Table 4.11. Summary of ORR Behavior of IN718 in 3.5% NaCl solution with varying pH

pH	Specimen	i_0 (mA/cm^2)	Tafel Slope (V/Dec)
1.25	AS-AM Received	3.70×10^{-15}	-0.094
	AS-AM (HT)	-	-
	AM-HIP Received	3.86×10^{-14}	-0.101
	AM-HIP (HT)	-	-
6.25	AS-AM Received	1.80×10^{-8}	-0.199
	AS-AM (HT)	3.91×10^{-8}	-0.203
	AM-HIP Received	1.33×10^{-8}	-0.195
	AM-HIP (HT)	2.99×10^{-8}	-0.212
12.25	AS-AM Received	1.60×10^{-7}	-0.189
	AS-AM (HT)	7.40×10^{-7}	-0.234
	AM-HIP Received	2.89×10^{-9}	-0.149
	AM-HIP (HT)	4.49×10^{-7}	-0.219
	Wrought Received	8.63×10^{-5}	-0.189
	Wrought (HT)	1.24×10^{-5}	-0.234

4.3.2 Galvanostatic Tests

Galvanostatic tests maintain a constant applied current and record changing potential. Overpotential is the difference between the experimentally observed potential and the calculated redox potential and is an important factor in evaluating the effectiveness of electrocatalysts and (E_{redox}). Galvanostatic tests conducted over 24 hours were used to assess overpotential at current densities of -10 mA/cm^2 and +10 mA/cm^2 to evaluate hydrogen evolution and oxygen evolution respectively. Resulting plots are shown in Figure 4.18(a)-(d).

The overpotentials found at -10 mA/cm^2 were generally consistent. SLM samples ranged from -0.48 to -0.43 V with the exception of sample AM-HIP which showed an overpotential of -0.62 V. Overpotentials in wrought samples were very similar and ranged from approximately -0.50 to -0.45 V.

The current took longer to steady at +10 mA/cm^2 in HIP samples and overpotentials ranged from 0.41 to 0.57 V in the SLM samples.

Wrought samples tested at +10 mA/cm^2 showed highly unstable potential plots in both received and heat treated samples.

General instability in the potential plots may suggest formed precipitates and defect density could act as catalytic sites for oxygen reduction.
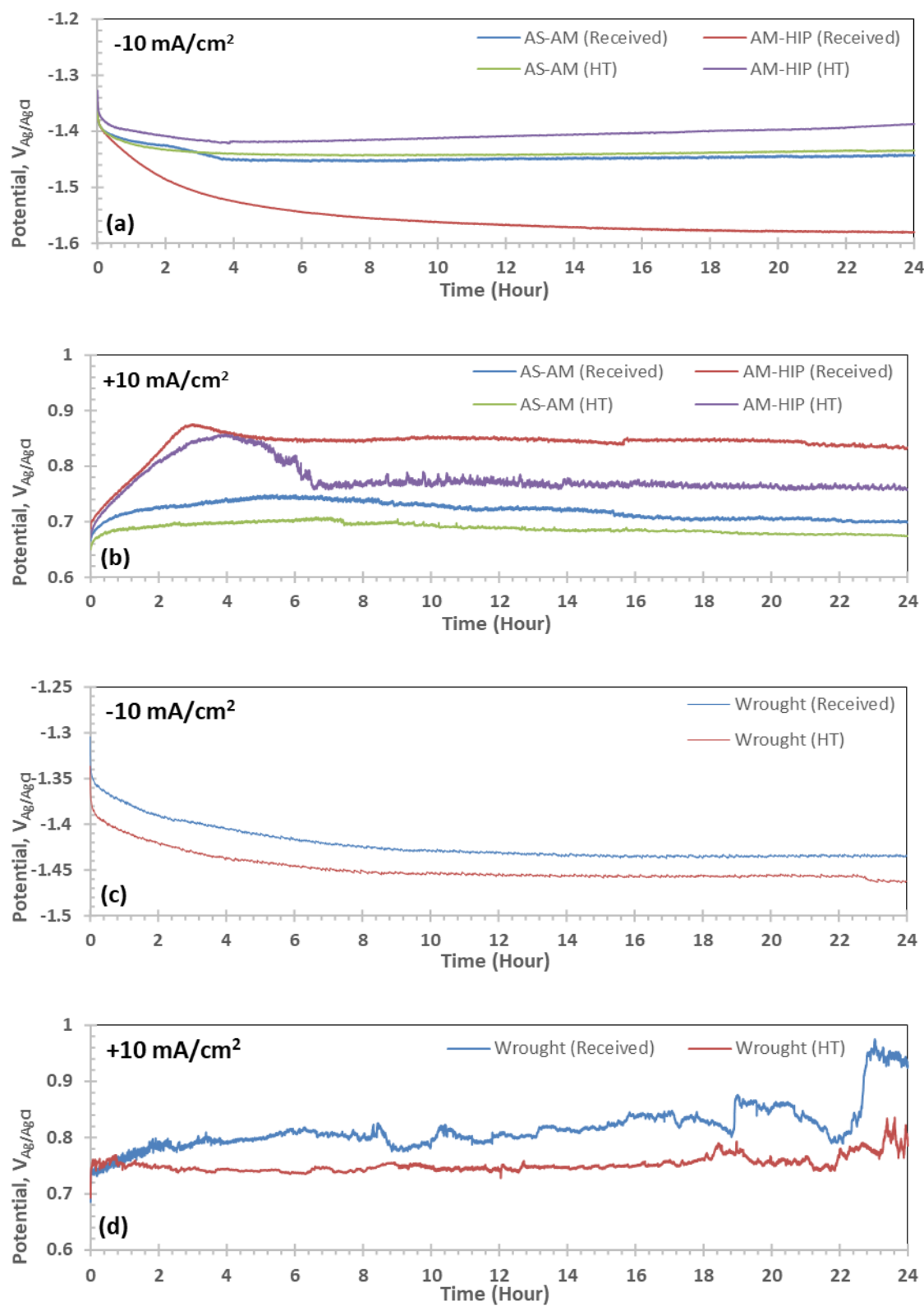
Figure 4.18. Galvanostatic plots for IN718 samples in 3.5% NaCl solution at pH=12.90. (a) SLM samples, applied current: -10 mA/cm², (b) SLM samples, applied current: +10 mA/cm², (c) Wrought samples, applied current: -10 mA/cm², (d) Wrought samples, applied current: +10 mA/cm²

4.3.3 Mott- Schottky Tests

MS analysis was performed on the samples after the 24-hour galvanostatic tests and the resulting plots are shown in Figures 4.3(a)-(b) and 4.4(a)-(b) for the SLM and wrought IN718 specimens respectively. Data is summarized in Tables 4.4 and 4.5 for SLM and wrought IN718 specimens respectively. Samples subjected to -10 mA/cm^2 (HER) showed both p and n-type semiconductive behavior, indicating a dual passive film formation on the surface. Those subjected to +10 mA/cm^2 only showed evidence of a p-type semiconduction. Though passivation is useful in corrosion resistance, it can be detrimental in electrocatalysts as the passive layer may block catalytic sites.

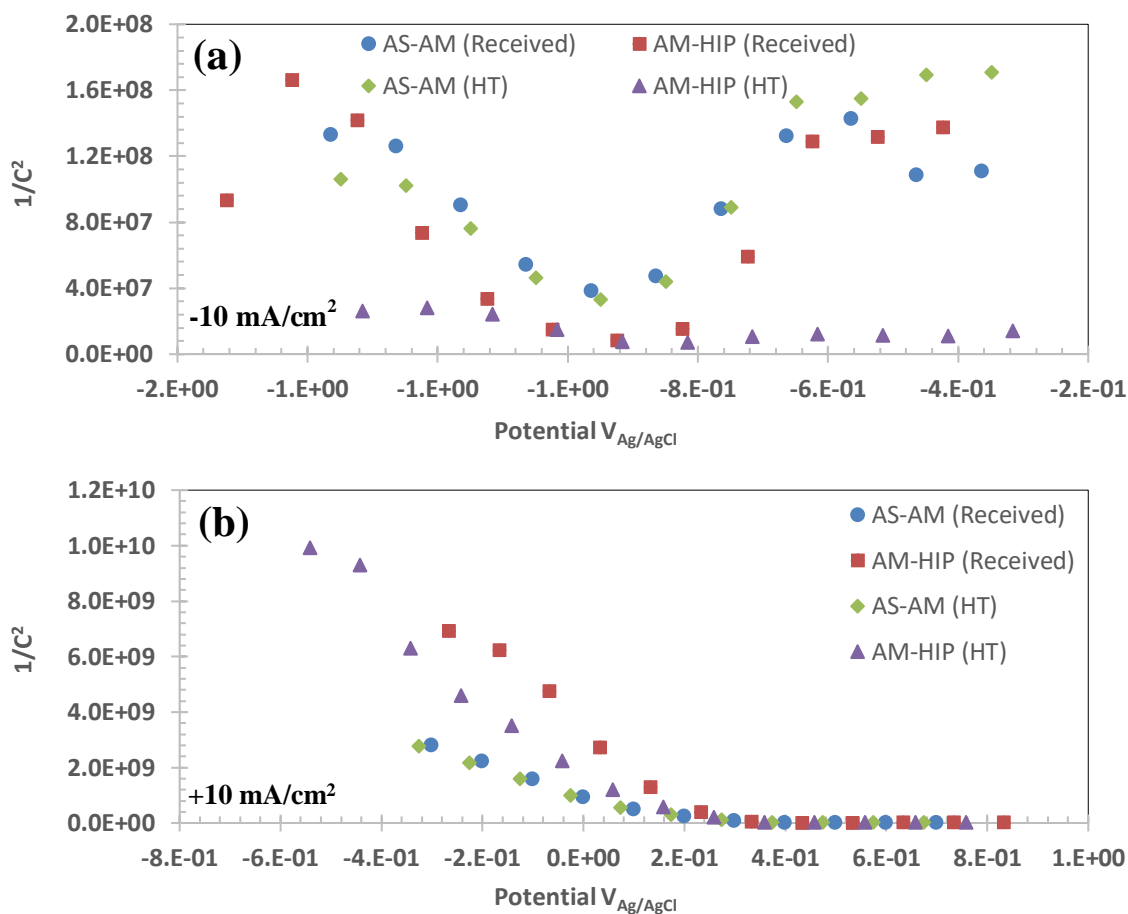In general, the charge carrier denstiy was lower in specimens that hand undergone HIP.

Figure 4.19. Mott-Schottky plots for SLM IN718 in 3.5% NaCl solution after 24-hour galvanostatic test. pH=12.90. (a) Applied current: -10 mA/cm^2, (b) Applied current: +10 mA/cm^2
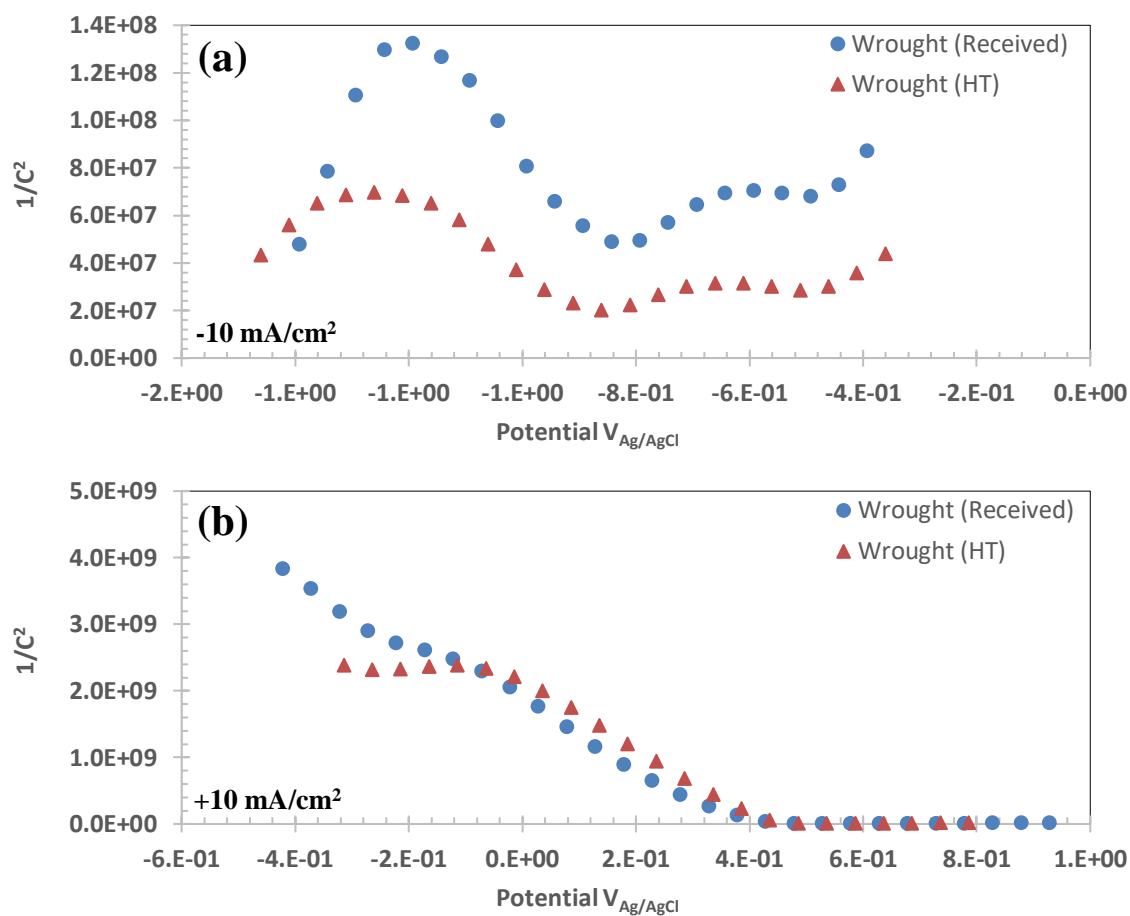
Figure 4.20. Mott-Schottky plots for wrought IN718 in 3.5% NaCl solution after 24-hour galvanostatic test. pH=12.90. (a) Applied current: -10 mA/cm2, (b) Applied current: +10 mA/cm2

Table 4.12. Data for Mott-Schottky analysis for SLM IN718 in 3.5% NaCl solution after 24 hour galvanostatic test. Applied current: -10 mA/cm^2

		Negative Slope			**Positive Slope**	
Specimen	**Slope**	**Charge Carrier Density (cm^{-3})**	**Flat Band Potential**	**Slope**	**Charge Carrier Density (cm^{-3})**	**Flat Band Potential**
AS-AM Received	-3.58E0+08	-3.04E+22	-0.915	4.26E+08	2.55E+22	-0.975
AS-AM (HT)	-2.78E+08	-3.90E+22	-0.89	6.40E+08	1.70E+22	-0.89
AM-HIP Received	-6.81E+08	-1.59E+22	-1.1	6.99E+08	1.56E+22	-0.81
AM-HIP (HT)	-8.34E+07	-1.30E+23	-0.825	7.20E+07	-1.51E+23	-1.03
Wrought Received	-2.94E+08	-3.69E+22	-0.705	1.52E+08	7.14E+22	-1.12
Wrought (HT)	-1.68E+08	-6.48E+22	-0.775	7.74E+07	1.40E+23	-1.09

Table 4.13. Data for Mott-Schottky analysis for SLM IN718 in 3.5% NaCl solution after 24 hour galvanostatic test. Applied current: $+10$ mA/cm^2

Specimen	Slope	Charge Carrier Density (cm^{-3})	Flat Band Potential
AS-AM Received	-6.42E+09	-1.69E+21	0.145
AS-AM (HT)	-5.91E+09	-1.84E+21	0.14
AM-HIP Received	-1.65E+10	-6.59E+20	0.21
AM-HIP (HT)	-1.26E+10	-8.65E+20	0.141
Wrought Received	-3.15E+09	-3.44E+21	0.345
Wrought (HT)	-5.30E+09	-2.05E+21	0.372

4.4 Conclusions

The Tafel slopes for the hydrogen evolution reaction (HER) were higher for the as-received samples than that of heat-treated counterparts in all the pH conditions.

Formation of γ' and γ" precipitates increased the catalytic activities of HER reaction. The increased HER activities of the heat treated samples could also be corroborated by the cyclic polarization results which showed decreased corrosion resistance after heat treatment.

The heat treated and HIPped samples showed lower Tafel slopes for HER than other sample conditions.

The Inconel 718 samples showed the lowest Tafel slopes in the alkaline pH condition.

The overpotentials for HER (at -10 mA/cm^2) were in the range of -0.48 to -0.43 V with the exception of sample AM-HIP which showed an overpotential of -0.62 V.

The overpotentials for OER (at +10 mA/cm^2) were in the range of 0.41 to 0.57 V.

The passive layers of the HIP samples showed lower charge carrier density than that of non-HIP specimens.

4.5 References

[1] M. M. Rashid, K. A. M. Mohammad, H. Naseem and M. Danish, "Hydrogen Production by Water Electrolysis: A Review of Alkaline Water Electrolysis, PEM Water Electrolysis and High Temperature Water," *International Journal of Engineering and Advanced Technology,* vol. 4, no. 3, pp. 80-93, February 2015.

[2] Y. Yan, B. Y. Xia, B. Zhao and X. Wang, "A Review on Noble-Metal-Free Bifunctional Heterogeneous Catalysits for Overall Electrochemical Water Splitting," *Journal of Materials Chemistry A,* vol. 4, no. 45, pp. 17587-17603, 2016.

[3] A. Eftekhari, "Electrocatalysts for Hydrogen Evolution Reaction," *International Journal of Hydrogen Energy,* vol. 42, no. 16, pp. 11053-11077, April 2017.

[4] V. Vij, S. Sultan, A. Harzandi, A. Meena, J. N. Tiwari, W.-G. Lee, T. Yoon and K. S. Kim, "Nickel–Based Electrocatalysts for Energy Related Applications: Oxygen Reduction, Oxygen Evolution, and Hydrogen Evolution Reactions," *ACS Catalysis,* vol. 7, no. 10, pp. 7196-7225, 2017.

[5] S. R. Ovshinsky, M. A. Fetcenko and J. Ross, "A Nickel Metal Hydride Battery for Electric Vehicles," *Science,* vol. 260, no. 5105, pp. 176-181, April 1993.

[6] W. Chen, Y. Jin, J. Zhao, N. Liu and Y. Cui, "Nickel-Hydrogen Batteries for Large-Scale Energy Storage," *PNAS,* vol. 115, no. 46, pp. 11694-11695, November 2018.

[7] N. K. Chaudhari, H. Jin, B. Kim and K. Lee, "Nanostructured Materials on 3D Nickel Foam as Electrocatalysts for Water Splitting," *Nanoscale,* vol. 9, no. 34, pp. 12231-12247, July 2017.

[8] W. Kreuter and H. Hofmann, "Electrolysis: The Important Energy Transformer In a World of Sustainable Energy," *International Journal of Hydrogen Energy,* vol. 23, no. 8, pp. 661-666, August 1998.